National Technical University of Athens

School of Naval Architecture and Marine Engineering

Division of Marine Structures

Shipbuilding Technology Laboratory

Diploma Thesis

Development of a robust Structural Health Monitoring framework for detecting damages in cylindrical geometries.

Nikolaos Cholevas

Thesis Supervisor: Konstantinos N. Anyfantis, Assistant Professor

ATHENS, DECEMBER 2022

Acknowledgments

This thesis concludes an academic journey in which much has changed for me personally and for the world in general. During these years I have gained important knowledge for my later life and my future professional career. Now, that I am on the verge of an uncertain future, I am both motivated and confident.

First and foremost, I want to thank my supervisor, Assistant Professor Konstantinos Anyfantis, for his invaluable advice, continuous support, and patience throughout my thesis studies. His vast knowledge and wealth of experience have inspired me throughout my academic research and daily life. Above all, his personal moral character and human traits asserted to be the foundation of an effective and thriving collaboration.

I would also like to thank the members of my supervisory committee, Professor Nicholas Tsouvalis and Dr. Christos Riziotis, from National Hellenic Research Foundation, for evaluating the quality of my thesis. Special thanks to Dr. Christos Riziotis, who gave me a unique opportunity and without whom it would not have been possible for me to have engaged in such an interesting thesis subject and so to expand my knowledge.

Also, I would like to thank Dr. Georgia Korompili from NHRF for her support and help and the valuable knowledge she shared with me during this time. Furthermore, thank …Mr. Guenter Mussbach, from Bayern Chemie/ MBDA Missile Systems, Germany, for discussions on SRMs health monitoring and propellants' materials properties.

I'd like to express my appreciation to my family. It would have been impossible for me to finish my studies without their tremendous understanding and encouragement over the last few years.

Finally, I want to express my gratitude to my friends and fellow students for the time we spent together during all these years and the knowledge they shared with me.

Abstract

Structural health monitoring (SHM) of Solid Rocket Motors (SRMs) using the finite element method to analyze strains is a powerful technique to evaluate the structural integrity of the SRM and consequently to prevent accidents that may have both economical and possibly human losses. The main purpose of this thesis is the detection of grain propellant cracks in the solid propellant of SRMs. The dimensions and the material properties of the three layers of the SRM are based on relevant literature. Two dimensions finite element models, with and without crack, are modeled and thermal loads are applied in order to simulate the post-production storage cooling of SRMs. Existing methods for structural health monitoring of SRMs are described. Hoop strains are collected from different areas of the SRM for the healthy model without crack and for the damaged model with crack and signal detection theory is employed to define the probability of detection and the probability of false alarm. It is shown that with one sensor it is possible to detect small grain propellant cracks with high probability of detection and very small probability of false alarm. Simulating the real-world case, an uncertainty for the material properties, particularly, the Young's modulus and the thermal expansion coefficient is suggested. 1000 different cases of different material properties are used to conduct finite element simulations of the SRM response in temperature cool down from curing temperature to storage temperature. The strain data are used to feed an artificial neural network for regression and predict the new hoop strains for a sample of 100.000 different material properties. It is concluded that in this case, one sensor placement was insufficient to detect grain propellant cracks with high probability of detection. Thus, the use of 3,6 and 9 sensors is suggested and further analyzed. It is proven that a system comprising 6 sensors in the middle of the insulation and outer of the cylinder was the most efficient.

Contents

List of Figures

List of Tables

I. Introduction

A solid propellant rocker motor or SRM is a rocket with a rockets engine that uses as fuel solid propellants. The earliest rockets were solid-fuel rockets powered by gunpowder and they were utilized in warfare by the Chinese, Persians, Mongols and Indians as beforetime as the 13th century [1].

Since solid-fuel rockets can stay in storage for an extended time without much propellant degradation and due to they consistently launch reliably, they have been frequently utilized in military applications for example missiles like METEOR (MBDA Missiles) [2][3]. So, today, SRMs are been used in advanced military operations and in space exploration as recently in ARTEMIS I space mission to moon which uses solid rocket busters [4][5].

A SRM is comprised by three main components, the casing, insulation and solid propellant. The objective of the case is to acquire the power being produced throughout the ignition of the solid propellant. This permits the power being produced to be directed in one direction (through a nozzle), so that the rocket produces a lot of thrust. In regard of this process the case must be capable of sustaining high temperatures and pressures. As a consequence of this, SRMs casing are constructed as cylindrical thin-walled pressure vessels. Materials for the casing vary from cardboard to steel alloys. The insulation represents as a layer of protection for the casing because it reduces the conduction of heat from the solid propellant throughout the operation. For the insulation, the main material that is used is an ethylene propylene diene monomer (EPDM) liner. The heart of an SRM is the solid propellant with high energy density that is being used to produce huge amounts of thrust when ignited. SRMs are usually made of composite propellants comprised of some chemical components as for example fuel, binders, oxidizers and curing agents and the most common material that is being used is ammonium perchlorate (AP) [5].

The main method of construction of the case is filament wound, which is being used to made high pressure vessels utilized in aerospace industries. Construct of filament wound composite vessels consists of: construction of composite material, of metallic polar boss and rubber lining design. A mixture of hoop and helical winding is employed. The layer sequence and angle of winding are based on construct and analysis. The shell part and ends have dissimilar layer sequence and thicknesses. Composite motor cases will get metallic end fittings. These end fitting are entrenched to the composite portion at the varied stages of manufacturing. Carbon fiber with epoxy resin scheme is mostly utilized as material [6].

Any part of a SRM is susceptible to developing flaws but the main cause of SRM failures is because of the nozzle and propellant. In this thesis, the main focus is the propellant and its interaction with the other part of the SRM due to its unique material properties and the its different flaws. The most ordinary defects and flaws are aging effects, grain propellant cracks and delamination between insulation and propellant. In this case, the main concern is the grain propellant cracks, because these cracks could be spreading all through the

operation of the SRM, increasing and concentrating pressure, causing unexpected case pressure, thrust evolution and eventually resulting in case fracture and failure of the motor due to a case burst or burn-through.

Structural health monitoring (SHM) entails the observation and analysis of a system over time utilizing periodically sampled response measurements to monitor changes to the material and geometric properties of engineering structures. A structural health monitoring for a SRM is important for various reasons. The most important of them is that it can prevent a possible crash of a solid rocket motor that carries astronauts and thus save human lives. Also, it rapidly reduces the costs of the associated industry. So, in this thesis, it is developed a structural health monitoring approach for an SRM based on Finite Element Method to detect flaws associated with grain propellant cracks.

At present, many researchers have tried to make a SHM model to detect grain propellant crack or delamination. Le et al. [7], have made a 2D model, using finite element software package ABAQUS, for the half section of the cylinder with sensors distributed spread equally along the inner surface of the case to study the impact of grain propellant cracks on radial stress of an SRM during freezing process. Using 3,4 and 6 sensors respectively, the minimum and maximum values of their readings is being collected and then their difference is being calculated and is being compared with the accuracy of the sensors. With this process, the 3,4 and 6 sensors systems can detect 18.8,9 and 7.6mm grain propellant cracks with 100% probability of detection.

Applying the same procedure, Le et al. [8] 3,4 and 6 sensors systems detect 15 degrees of debonding, on the propellant insulation interface, for the first 2 and 9 degrees for the last one with 100% probability of detection. Also, a second method has been recommended that compares the healthy model with damaged model with debonding radial stress. In this way, the debonding degree detection is increased from 15° to 12° for 100% probability of detection.

Liu et al. [9] proposed a deep convolutional neural network that predicts the grain propellant crack length and the delamination angle with root mean square error 3.2mm and 2.0° respectively from the 2D model constructed in finite element software package ABAQUS.

In this thesis, a finite element method has been used to investigate the effect of grain propellant cracks on the SRM with an artificial neural network (ANN) for regression of the uncertainty propagation of the material properties and the application of the detection theory to the SRM, using the hoop strains of different areas of the cylinder both from the FE model and the surrogate model.

II. Theoretical Framework

a. Uncertainty Quantification (UQ)

The Monte Carlo method is a type of simulation, which most common goal, of using this procedure, is to predict specific parameters and probability distributions of random variables whom the values are based on relations with random variables with defined probability distributions [10]. In this work we are interested in the forward probabilistic UQ framework, which is also known as uncertainty propagation. This direction is of particular interest for the case where we want to propagate the uncertainty involved in the material parameters to the strain field of the SRM. Let's define the basic random vector $\mathbf{X} \in D_{\mathrm{X}}$ with $D_{\mathrm{X}} \subset \mathbb{R}^{d_0}$ and $d_0 \in \mathbb{Z}^+$ that includes d_0 material parameters, i.e. Young's modulus and coefficient of thermal expansion for the three layers. When the statistical process is realized we observe a particular realization of $\mathbf{X} = X$ with $X = \left\{x_1, x_2, ..., x_{d_0}\right\}^{\mathrm{T}}$. A probabilistic description of $\mathbf{X}$ is expressed through the joint probability density function as $\mathbf{X} \sim p_{\mathbf{X}}\left(\mathbf{X} = X; \boldsymbol{\Theta}_{\mathrm{X}}\right)$ with a known functional form and a vector that contains the population parameters, $\boldsymbol{\Theta}_{\mathrm{X}} \in D_{\boldsymbol{\Theta}_{\mathrm{X}}}$ with $D_{\boldsymbol{\Theta}_{\mathrm{X}}} \subset \mathbb{R}^{d_1}$ and $d_1 \in \mathbb{Z}^+$. Integer d_1 indicates the number of parameters involved in the probabilistic model $p_{\mathbf{X}}(\cdot)$. If the components of $\mathbf{X}$ are statistically uncorrelated and treated as independent events, then the pdf of $\mathbf{X}$ may be written as the product of its marginal pdfs as:

$$p_{\mathbf{X}}\left(\mathbf{X} = X; \boldsymbol{\theta}_{\mathrm{X}}\right) = \prod_{i=1:d} p_{\mathbf{x},i}(X(d); \boldsymbol{\theta}_d), \text{ with } \boldsymbol{\theta}_d \subset \boldsymbol{\theta}_X \tag{1}$$

The relation between the material parameters and the strain response is described through a computational model [11]

$$M : \mathbf{X} = X \mapsto \mathbf{E} = E \tag{2}$$

that receives a realization of $\mathbf{X} = X$ and returns the corresponding $\mathbf{E} = E$ outcome in a deterministic fashion. The relation $E = M(X)$ describes a real-value function that operates over X. Let's consider the random vector $\mathbf{E} \in D_{\mathrm{E}}$ with $D_{\mathrm{E}} \subset \mathbb{R}^{d_2}$ and $d_2 \in \mathbb{Z}^+$ that arranges d_2 strain components (features). As before, when the statistical process is realized we observe a particular realization of $\mathbf{E} = E$ with $E = \left\{\varepsilon_1, \varepsilon_2, .., \varepsilon_i, .., \varepsilon_{d_2}\right\}^{\mathrm{T}}$. The aim of the uncertainty propagation is to estimate the probability distribution of $\mathbf{E}$, as $p_{\mathrm{E}}\left(\mathbf{E} = E; \boldsymbol{\theta}_{\mathrm{E}}\right)$, with $\boldsymbol{\theta}_{\mathrm{E}} \in D_{\boldsymbol{\theta}_{\mathrm{E}}}$, $D_{\boldsymbol{\theta}_{\mathrm{E}}} \subset \mathbb{R}^{d_3}$ and $d_3 \in \mathbb{Z}^+$. The mean vector within $\boldsymbol{\theta}_{\mathrm{E}}$ is estimated as

$$\mu_{\mathrm{E}}(i)=\mathrm{E}[\varepsilon_i]=\mathrm{E}\left[M(X)_i\right]=\int_{D_{\mathrm{X}}} M(X)_i\, p_{\mathbf{X}}(\mathbf{X}=X;\boldsymbol{\theta}_{\mathrm{X}})\,\mathrm{d}X \tag{3}$$

and the component variances, are given as:

$$\sigma^2_{\mathrm{E}}(i)=\mathrm{Var}[\varepsilon_i]=\mathrm{Var}[M_i]=\mathrm{E}\left[M_i^2\right]-\mathrm{E}[M_i]^2 \tag{4}$$

The covariances are formally described as:

$$\mathrm{cov}\left[\varepsilon_i\varepsilon_j\right]=\mathrm{E}\left[\varepsilon_i\varepsilon_j\right]-\mathrm{E}[\varepsilon_i]\mathrm{E}\left[\varepsilon_j\right] \text{ with } i\neq j \tag{5}$$

Eq. (15) to (17) are analytically intractable and as such one needs to employ statistical simulations to tackle the problem. Monte Carlo Simulation (MCS) is a robust method that is based on the idea of random sampling. In practice, *n* realizations are sampled from $p_{\mathbf{X}}(\mathbf{X}=X;\boldsymbol{\theta}_{\mathrm{X}})$, $\left\{\left(x_1,...,x_{\mathrm{d}_0}\right)_{k=1},\left(x_1,...,x_{\mathrm{d}_0}\right)_{k=2},....,\left(x_1,...,x_{\mathrm{d}_0}\right)_{k=n},k=1,2,...,n\right\}$ which are then fed forward to *M*(*X*) in order to produce $\left\{\left(\varepsilon_1,...,\varepsilon_{\mathrm{d}_2}\right)_{k=1},\left(\varepsilon_1,...,\varepsilon_{\mathrm{d}_2}\right)_{k=2},....,\left(\varepsilon_1,...,\varepsilon_{\mathrm{d}_2}\right)_{k=n},k=1,2,...,n\right\}$ outcome instances. The latter are collected and statistically analyzed. It has been shown that if a large number of random samples are simulated, then the method can achieve a complete description of the statistical behavior of the output random vector **E**. The epistemic uncertainty that is introduced because of the sampling process is quantified through formal inferential statistics. According to the Central Limit Theorem, we can write the following probability statement for the population mean, μ_i, that is estimated from a formal statistical inference applied on the sample mean component, $\overline{\varepsilon_i}$:

$$\Pr\left[\overline{\varepsilon}_i-t_{(n-1,1-\alpha/2)}\frac{s_i}{\sqrt{n}}\leq\mu_{\mathrm{E}}(i)\leq\overline{\varepsilon}_i+t_{(n-1,1-\alpha/2)}\frac{s_i}{\sqrt{n}}\right]=1-\alpha \tag{6}$$

where (1-α) is the desired confidence level and $t_{n-1}(\cdot)$ is the critical value of the Student's t-distribution with *n*-1 degrees of freedom. The sample size is denoted as *n*. Magnitude $s_i/\sqrt{n}$ is called the standard error and is equal to the standard deviation of the normally distributed sample average. The preceding statement is valid for cases where the response random variable ε_i is normally distributed or not highly skewed. In a similar fashion, a confidence interval may be constructed for the variance, $\overline{\varepsilon_i}$, based on the below probabilistic statement:

$$\Pr\left[\frac{n-1}{\chi^2_{(n-1,\alpha/2)}}s_i^2\leq\sigma^2_{\mathrm{E}}(i)\leq\frac{n-1}{\chi^2_{(n-1,1-\alpha/2)}}s_i^2\right]=1-\alpha \tag{7}$$

where $\chi^2_{n-1}(\cdot)$ is the critical value of the Chi-squared distribution with *n*-1 degrees of freedom.

The Monte Carlo estimators converge always to the real parameters with a prediction error being reduced as the sample size increases. It is typical to expect that ~10^5 realizations are required in order to have a prediction error less than 5% in the QoI for a 95% confidence interval.

b. Surrogate Modeling

The computationally demanding statistical simulation scheme requires the employment of surrogate modelling in order for the process to time affordable. Surrogate modes are data-driven models that are usually generated from physics-based models. Their main objective is to substitute computationally intensive simulations with fast and accurate models. In principle, surrogate modeling is a regression problem. In this direction, a relatively limited number of simulations is performed and the obtained response data are used for training a statistical model. The idea is to identify the latent statistical structure of the synthetic observations and accordingly construct the model that best describes the data generation process. Depending on the degree of non-linearity of the mapping function (Eq. (2)) a different modeling strategy may be employed. Machine learning tools suit well this purpose. In this work we decided to employ a dense multilayer perceptron (Artificial Neural Network - ANN) to act as the surrogate model. The contribution of artificial intelligence on many research fields is critical and ANN help on making decisions on models with a lot of data. They can be used for regression or classification.

ANN for regression is combined of 3 layers: input layer, which picks ups signals and passes them to the next layer, hidden layer, which does all kinds of calculating and feature extraction and output layer, which delivers the final results. The input layer consists of d_0 nodes that each one receives an instance (or realization) of the material parameters, $X = \left\{x_1, x_2, ..., x_{d_0}\right\}^{\mathrm{T}}$. The output layer consists of d_2 nodes and each node is associated with a specific strain feature, $E = \left\{\varepsilon_1, \varepsilon_2, ..., \varepsilon_{d_2}\right\}^{\mathrm{T}}$. Artificial neural networks are a sufficient machine learning method because of their flexibility to change weightings, deviations, hidden values and the number of neurons and the number of the hidden layers so a good regression model is achieved [12][13]. During the supervised learning stage, a training set $[X, E]_n$ of n instances is used in order to train the weights and biases associated with the model's architecture. The number of these quantities are defined within the hidden layers implicitly and are considered as hyperparameters that the user needs to set. The activation functions need to be as well defined by the user. The training process is in fact an optimization process which ends once a prediction error is minimized to an acceptable level or a number of epochs is reached.

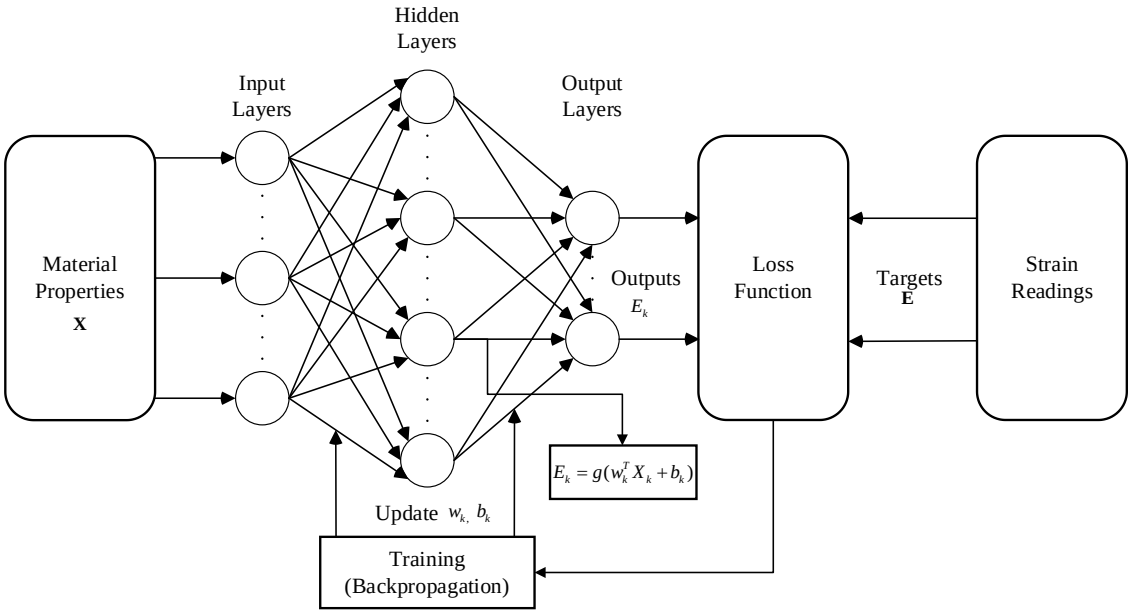

Figure 1: ANN architecture.

c. Detection Theory

First of all, in this part of the thesis is very useful to explain the base principals of the classical hypothesis testing:

Classical Hypothesis Testing [14]

A statistical hypothesis is an assertion or conjecture one or more populations. The hypothesis testing consists of two hypotheses, the null Hypothesis H_0, which refers to the hypothesis we want to test and the alternative hypothesis H_1 where it led us the rejection of the alternative hypothesis usually represents the question to be answered or the theory to be tested. The null hypothesis nullifies or opposes the alternative hypothesis and is often the logical complement to the alternative hypothesis.

In these hypotheses are included and some errors in our decisions, which are:

- Type I error: Rejection of the null hypothesis when it is true.
- Type II error: Nonrejection of the null hypothesis when it is false.

In the table below there are concluded the possible results of hypothesis testing:

Table 1: Possible results of Hypothesis Testing

	H_0 **is true**	H_0 **is false**
Do not Reject H_0	Correct Decision	Type II error
Reject H_0	Type I error	Correct Decision

Moving forward, although detection theory was initially developed to address signal detection problems within information and communication technology (radars, telecom etc.), its strength was quickly acknowledged by the SHM community. The involved statistical discipline and technical ingredients fit well to the damage identification problem, either if treated as a binary (Healthy or Damaged) or as a multi-class problem, with the former acting as the basis in this work. Signal discrimination is based on the likelihood ratio test, which is in principle a statistical hypothesis test constructed over two competing hypotheses. We define the null hypothesis as the Healthy state of the RSM ($\mathrm{H}_0 \equiv \mathrm{H}$), i.e. its geometry being intact. We are interested in testing this null hypothesis against the alternative hypothesis of the SRM being damaged ($\mathrm{H}_1 \equiv \mathrm{D}$), which translates into the existence of a grain propellant crack of minimum length equal to α_{cr}. The sensor readings are arranged in a real-valued vector $\mathbf{X}_{\mathrm{test}} \in \mathbb{R}^d$, with $d \in \mathbb{Z}$ being the number of installed sensors. Each component in $\mathbf{X}_{\mathrm{test}}$ may be considered as an average timeseries post-processed within the data acquisition system, $\mathbf{x}_{\mathrm{test}}[i] = \frac{1}{t_{\mathrm{n}}} \sum_{t=1}^{t_{\mathrm{n}}} \mathbf{x}_{\mathrm{test}}[i]_t$. We need to associate vector $\mathbf{X}_{\mathrm{test}}$ with one of the two defined SRM states (H or D) and this action is performed by comparing the probabilistic support (likelihood) provided by their statistical structure. The *d*-dimensional multivariate probability density function (PDF) that corresponds to the healthy state is denoted as $f_{\mathrm{H}}(\cdot;\boldsymbol{\Theta}_{\mathrm{H}})$ and the respective model for the damaged state is denoted as $f_{\mathrm{D}}(\cdot;\boldsymbol{\Theta}_{\mathrm{D}})$. The distribution parameters are deterministic yet unknown values $\boldsymbol{\Theta}_{\mathrm{H}}, \boldsymbol{\Theta}_{\mathrm{D}} \in \mathrm{D}_{\boldsymbol{\Theta}}, \mathrm{D}_{\boldsymbol{\Theta}} \subset \mathbb{R}^{d_\Theta}$ with $d^{\Theta} \in \mathbb{Z}$, and they will be estimated from sample statistics or defined from deterministic signals within noise. The competing hypotheses may be formally written as:

$$\begin{cases} \mathrm{H}_0 \equiv \mathrm{H}: & \mathbf{X}_{\mathrm{test}} \sim f_{\mathrm{H}}(\mathbf{x}_{\mathrm{test}};\boldsymbol{\Theta}_{\mathrm{H}}) \\ \mathrm{H}_1 \equiv \mathrm{D}: & \mathbf{X}_{\mathrm{test}} \sim f_{\mathrm{D}}(\mathbf{x}_{\mathrm{test}};\boldsymbol{\Theta}_{\mathrm{D}}) \end{cases} \tag{8}$$

The Neyman-Pearson detector [15] asserts that the reading $\mathbf{X}_{\mathrm{test}}$ is associated with the Damage state if the probabilistic support for this event to occur is higher than the probabilistic support of its counterpart event (Healthy state) to occur or mathematically given by the conditional probabilities as:

$$\Pr[\mathrm{D}|\mathbf{X}_{\mathrm{test}}] > \Pr[\mathrm{H}|\mathbf{X}_{\mathrm{test}}] \tag{9}$$

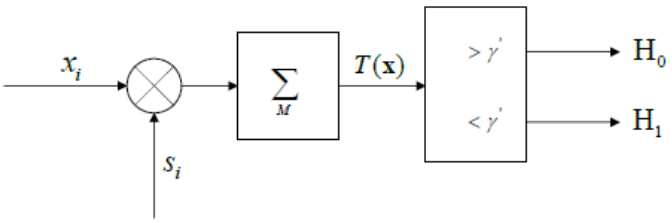

Figure 2: Matched Filter of Neyman-Pearson detector.

By applying the Baye's rule into Eq. (9) for the nominator and denominator, the likelihood ratio test is written as:

$$\mathrm{L}\left(\mathbf{x}_{\text{test}};\boldsymbol{\Theta}_{\mathrm{H}},\boldsymbol{\Theta}_{\mathrm{D}}\right)\equiv\frac{f_{\mathrm{D}}\left(\mathbf{x}_{\text{test}};\boldsymbol{\Theta}_{\mathrm{D}}\right)}{f_{\mathrm{H}}\left(\mathbf{x}_{\text{test}};\boldsymbol{\Theta}_{\mathrm{H}}\right)}>\gamma \tag{16}$$

It is evident that the detector's accuracy is controlled by the assigned probabilistic structure and the estimated corresponding parameters ($\boldsymbol{\Theta}_{\mathrm{H}},\boldsymbol{\Theta}_{\mathrm{D}}$), which are directly related to the specified sensor topology and architecture. The level of achieved accuracy is proportional to the discriminant strength or richness in information content provided by the selected features. This is in fact a problem of optimal sensor placement and is in the heart of this research. The likelihood ratio partitions the feature space in two regions by introducing a threshold per feature. However, the binary decision that revolves around to reject or to fail-to-reject the null hypothesis is associated with a risk of mistakenly making a decision in favor of a hypothesis that is not the state of nature. This level of risk is quantified through probabilistic assignments to the involved errors and reflects well known Type I and Type II errors in the classical hypothesis testing setting.

Within the framework of detection theory, the complement probability associated with Type II error defines the probability of detection, P_{D}, and is estimated from the below series of integrals:

$$P_{\mathrm{D}}=\int_{\mathbf{x}_\gamma:L\left(\mathbf{x}_\gamma\right)=\gamma}^{+\infty}f_{\mathrm{D}}\left(\mathbf{x};\boldsymbol{\Theta}_{\mathrm{D}}\right)\mathrm{d}\mathbf{x} \tag{11}$$

Type I error is equivalent to the probability of false alarm and is given by:

$$P_{\mathrm{FA}}=\int_{\mathbf{x}_\gamma:L\left(\mathbf{x}_\gamma\right)=\gamma}^{+\infty}f_{\mathrm{H}}\left(\mathbf{x};\boldsymbol{\Theta}_{\mathrm{H}}\right)\mathrm{d}\mathbf{x} \tag{12}$$

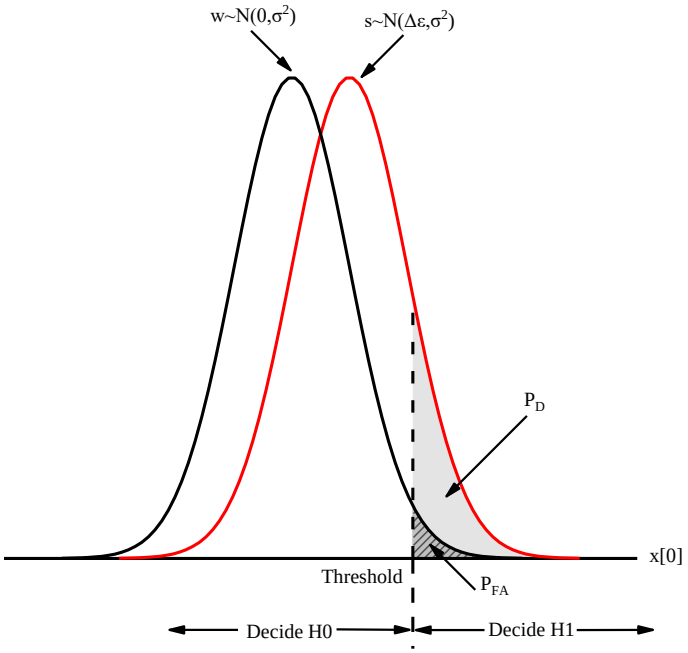

Figure 3: Hypothesis Testing.

The instance $\mathbf{X}_\gamma$ corresponds to the partition boundaries and sets the lower limit of the integrals. Having defined the performance metrics, the aim is to optimize the detector's accuracy by maximizing the probability of detection and minimizing the probability of false alarm. However, these two objectives are competing each other in the sense that there does not exist such a utopia point that optimizes both metrics at the same time. However, the Neyman-Pearson detector, i.e., the likelihood ratio test in Eq. (10), is an optimal criterion, in the sense that for a specified level probability of false alarm the detector maximizes the probability of detection.

Two cases are of particular interest under this analysis. The first relates to the reference condition where the material parameters are deterministic quantities and randomness in the strain readings comes solely from measurement noise, which is assumed to follow a zero-mean, homogeneous and uncorrelated Gaussian process with variance σ^2. This corresponds to the case where a deterministic signal is hidden in White Gaussian Noise (WGN). We may reformulate the hypotheses in order to reflect the typical framing where the null hypothesis refers at the noise only state of nature and the alternative hypothesis refers at signal in noise state of nature. The absence of a signal indicates that the SRM remains healthy, whereas the identification of a signal (in noise) indicates the existence of a grain propellant crack. The PDF is described as $f_{\mathrm{H}}(\cdot) = f_{\mathrm{D}}(\cdot) = \mathrm{N}(\cdot)$ and the parameter vectors are given as $\boldsymbol{\Theta}_{\mathrm{H}} = \{\mathbf{0}_d, \boldsymbol{\Sigma}_{dxd}\}$ and $\boldsymbol{\Theta}_{\mathrm{D}} = \{\boldsymbol{\Delta\varepsilon}_d, \boldsymbol{\Sigma}_{dxd}\}$,

where $\mathbf{0}_d$ is the *d*-dimensional zero mean vector, $\mathbf{\Sigma}_{dxd} = \sigma^2 \cdot \mathbf{I}_{dxd}$ is the *d* x *d*- dimensional covariance matrix and $\mathbf{\Delta\varepsilon}_d$ is the *d*-dimensional mean vector that contains the deterministic signal. In the case where only one feature is considered, i.e. only one sensor is installed, i.e. *d* = 1, then the problem turns out to be univariate. The analytical solution to the problem is provided by the equation below:

The equation (10) we can rewrite it as:

$$\frac{\frac{1}{(2\pi\sigma^2)^{N/2}}\exp[-\frac{1}{2\sigma^2}\sum_{a=0}^{N-1}(x[a]-A)^2]}{\frac{1}{(2\pi\sigma^2)^{N/2}}\exp[-\frac{1}{2\sigma^2}\sum_{a=0}^{N-1}x^2[a]]} > \gamma \quad (13)$$

, where A=Δε(a).

If we logarithm both side we get:

$$-\frac{1}{2\sigma^2}(-2A\sum_{a=0}^{N-1}x[a]+NA^2) > \ln(\gamma) \quad (14)$$

Which can be simplified to:

$$\frac{A}{\sigma^2}\sum_{a=0}^{N-1}x[a] > \ln(\gamma)+\frac{NA^2}{2\sigma^2} \quad (15)$$

And finally, we have:

$$\frac{1}{N}\sum_{a=0}^{N-1}x[a] > \frac{\sigma^2}{NA}\ln(\gamma)+\frac{A}{2} = \gamma' \quad (16)$$

To determine the detection performance, we first note that the test statistic $T(x) = \frac{1}{N}\sum_{a=0}^{N-1}x[a]$ is Gaussian under each hypothesis. The means and variances are:

$$E(T(x);H_0) = E(\frac{1}{N}\sum_{a=0}^{N-1}w[a]) = \frac{1}{N}\sum_{a=0}^{N-1}E(w[a]) = 0 \quad (17)$$

With the same way we get:

$$E(T(x);H_1) = A \quad (18)$$

And:

$$\mathrm{var}(T(x);H_0)=\mathrm{var}(\frac{1}{N}\sum_{a=0}^{N-1}w[a])=\frac{1}{N^2}\sum_{a=0}^{N-1}\mathrm{var}(w[a])=\frac{\sigma^2}{N} \quad (19)$$

Similarly, we get:

$$\mathrm{var}(T(x);H_1)=\frac{\sigma^2}{N} \quad (20)$$

So, we get:

$$T(x)\sim\left\{\begin{array}{ll} N(0,\frac{\sigma^2}{N}) & \text{under } H_0 \\ N(A,\frac{\sigma^2}{N}) & \text{under } H_1 \end{array}\right\} \quad (21)$$

And then:

$$P_{FA}=\Pr(T(x)>\gamma';H_0)=Q(\frac{\gamma'}{\sqrt{\frac{\sigma^2}{N}}}) \quad (22)$$

, where Q(x)=1-Φ(x).

The threshold is found:

$$\gamma'=\sqrt{\frac{\sigma^2}{N}}Q^{-1}(P_{FA}) \quad (23)$$

We can relate P_D to P_{FA} through the below equations:

$$P_{D(a)}=Q(\frac{\sqrt{\frac{\sigma^2}{N}}Q^{-1}(P_{FA})-A}{\sqrt{\frac{\sigma^2}{N}}})=Q(Q^{-1}(P_{FA})-\sqrt{\frac{NA^2}{\sigma^2}}) \quad (24)$$

And finally for this thesis case, for N=1 and A=Δε(a), we get:

$$P_{\mathrm{D}}=Q\left(Q^{-1}\left(P_{\mathrm{FA}}\right)-\sqrt{\frac{\Delta\varepsilon^2}{\sigma^2}}\right) \quad (25)$$

where $Q(\cdot)=1-\Phi(\cdot)$ is the Q-function and $Q^{-1}(\cdot)=\sqrt{2}\,\mathrm{erfinv}(1-2\cdot)$ is its inverse mapping. The preceding equation gets as input the magnitude of the informative feature, $\Delta\varepsilon$, the noise level σ^2 and the P_{FA}

level of interest and delivers the maximum probability of detection when that is a characteristic of the detection system.

In the case where variability in the material parameters is taken into consideration, then the dispersion around the mean is not guided by the statistical structure of the noise but by the degree of variability of the basic random variables which consequently propagates to the strain response (features). By considering that normality in the data holds, the probabilistic model for the features in the healthy state is $f_{\mathrm{H}}\left(\cdot;\boldsymbol{\Theta}_{\mathrm{H}}\right)=\mathrm{N}\left(\cdot;\mu_{\mathrm{H}},\sigma_{\mathrm{H}}^{2}\right)$ and the corresponding model for the features in the damaged state is $f_{\mathrm{D}}\left(\cdot;\boldsymbol{\Theta}_{\mathrm{D}}\right)=\mathrm{N}\left(\cdot;\mu_{\mathrm{D}},\sigma_{\mathrm{D}}^{2}\right)$. For one strain sensor (d = 1), as before, Eq. (25) no longer applies since ($\sigma_{\mathrm{H}}^{2}\neq\sigma_{\mathrm{D}}^{2}$) and the estimation of the probability of detection needs to be separated in a two-step process.

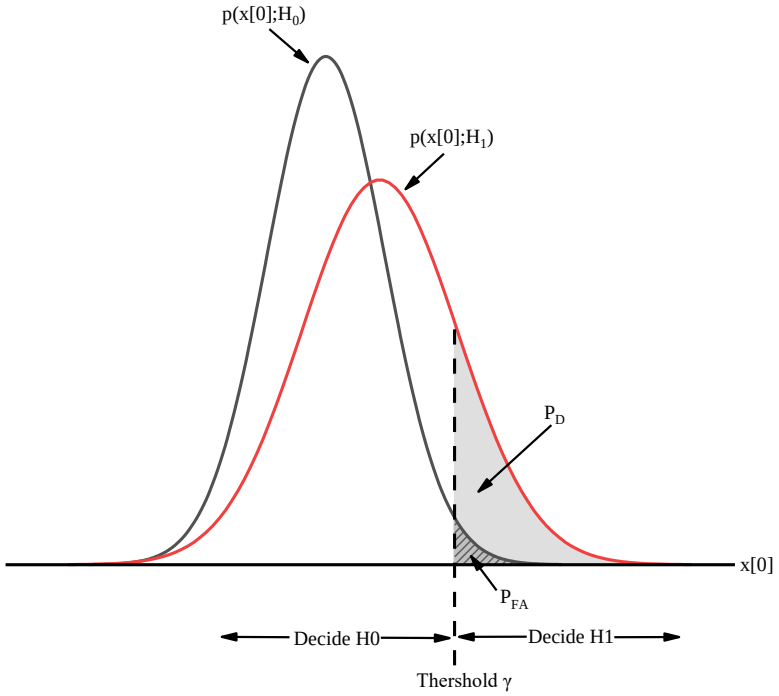

Figure 4: Hypothesis Testing for different standard deviation.

We first obtain the threshold, γ, that results in the desired probability of false alarm as:

$$\mathrm{P}_{\mathrm{FA}}=1-\Phi\left(\frac{\gamma-\mu_{\mathrm{H}}}{\sigma_{\mathrm{H}}}\right)=Q\left(\frac{\gamma-\mu_{\mathrm{H}}}{\sigma_{0}}\right) \tag{26}$$

and solving with respect to the threshold we obtain:

$$\gamma = Q^{-1}\left(\mathrm{P}_{\mathrm{FA}}\right)\cdot\sigma_{\mathrm{H}} + \mu_{\mathrm{H}} \tag{27}$$

Then the probability of detection may easily be obtained as:

$$\mathrm{P}_{\mathrm{D}} = Q\left(\frac{\gamma - \mu_{\mathrm{D}}}{\sigma_{\mathrm{D}}}\right) \tag{28}$$

If we substitute Eq. (8) in Eq. (9) then the system's characteristic performance may be derived from:

$$\mathrm{P}_{\mathrm{D}} = Q\left(\frac{Q^{-1}\left(\mathrm{P}_{\mathrm{FA}}\right)\cdot\sigma_{\mathrm{H}} + \mu_{\mathrm{H}} - \mu_{\mathrm{D}}}{\sigma_{\mathrm{D}}}\right) \tag{29}$$

When $d \neq 1$, then the problem revolves around a multivariate normal model with $f_{\mathrm{H}}\left(\cdot;\boldsymbol{\Theta}_{\mathrm{H}}\right) = \mathrm{N}\left(\cdot;\mathbf{0},\boldsymbol{\Sigma}_{\mathrm{H}}\right)$ and $f_{\mathrm{D}}\left(\cdot;\boldsymbol{\Theta}_{\mathrm{D}}\right) = \mathrm{N}\left(\cdot;\boldsymbol{\Delta\varepsilon},\boldsymbol{\Sigma}_{\mathrm{D}}\right)$ where $\boldsymbol{\Sigma}_{\mathrm{H}}$ and $\boldsymbol{\Sigma}_{\mathrm{D}}$ is the covariance matrix for the healthy and damaged state, respectively.

$$\mathrm{L}\left(\mathbf{x}_{\text{test}};\boldsymbol{\Theta}_{\mathrm{H}},\boldsymbol{\Theta}_{\mathrm{D}}\right) \equiv \frac{\sqrt{\left|\boldsymbol{\Sigma}_{\mathbf{D}}\right|}\exp\left[-\frac{1}{2}\left(\mathbf{x}_{\text{test}} - \boldsymbol{\Delta\varepsilon}\right)^{\mathrm{T}}\boldsymbol{\Sigma}_{\mathrm{D}}^{-1}\left(\mathbf{x}_{\text{test}} - \boldsymbol{\Delta\varepsilon}\right)\right]}{\sqrt{\left|\boldsymbol{\Sigma}_{\mathbf{H}}\right|}\exp\left[-\frac{1}{2}\left(\mathbf{x}_{\text{test}}\right)^{\mathrm{T}}\boldsymbol{\Sigma}_{\mathrm{H}}^{-1}\left(\mathbf{x}_{\text{test}}\right)\right]} \tag{30}$$

It is evident that the performance of the detectors depends solely on the magnitude of the parameters $\boldsymbol{\Theta}_{\mathrm{H}},\boldsymbol{\Theta}_{\mathrm{D}},\boldsymbol{\Delta\varepsilon}$ and these will be defined from a statistical simulation based on a deterministic model. The analytical description for the system's characteristic is intractable and a numerical approach is required in order to estimate the probability of detection given the probability of false alarm. Within the Neyman-Pearson setting one may solve an optimization problem in order to initially obtain the threshold that results in the specified probability of false alarm, i.e. $\gamma_{\mathrm{MC}} = \arg\min_{\gamma}\left(\ln\left(P_{\mathrm{FA}} - P_{\mathrm{FA}}\left(\gamma\right)\right)^{2}\right)$. Then use this threshold within a Monte Carlo Simulation (discussed in sub-section 2.2) in order to obtain the optimal probability of detection. However, in this work, since the main interest is to construct the ROC curve, we evaluated the P_{FA} - P_{D} pair for different specified values of the threshold. This is performed by passing through Eq. (30) a *n*-sized sample (referred as training set) with a given threshold and count the true negatives (*TN*) and false positives (*FP*). Then the following Monte Carlo point estimators may be used:

$$P_{\mathrm{D}} = TN/n \text{ and } P_{\mathrm{FA}} = FP/n \tag{31}$$

III. Case Study

a. Problem Definition

In this paper, the cylindrical geometry of the SRM allows the problem to be regarded as axisymmetric or plane strain allowing for 2D modeling in the r-z plane and r-θ plane, respectively. Since there is interest to model a crack initiating and propagating along a radial direction at a random yet controlled angle θ, the problem was modeled as plane strain, as shown in Figure 4. As shown in Figure 4, the structure consists of case, insulation and grain or grain propellant. The inner and outer dimensions of radius of grain propellant is 203.2mm and 406.4mm, respectively. The thickness of insulation is 2.54mm and the thickness of case is 3.175mm [16]. Especially in this study, it was modeled only the one quarter of the cylinder, as shown in Figure 4, because it was considered that the results on the remaining cylinder is the same due to symmetry.

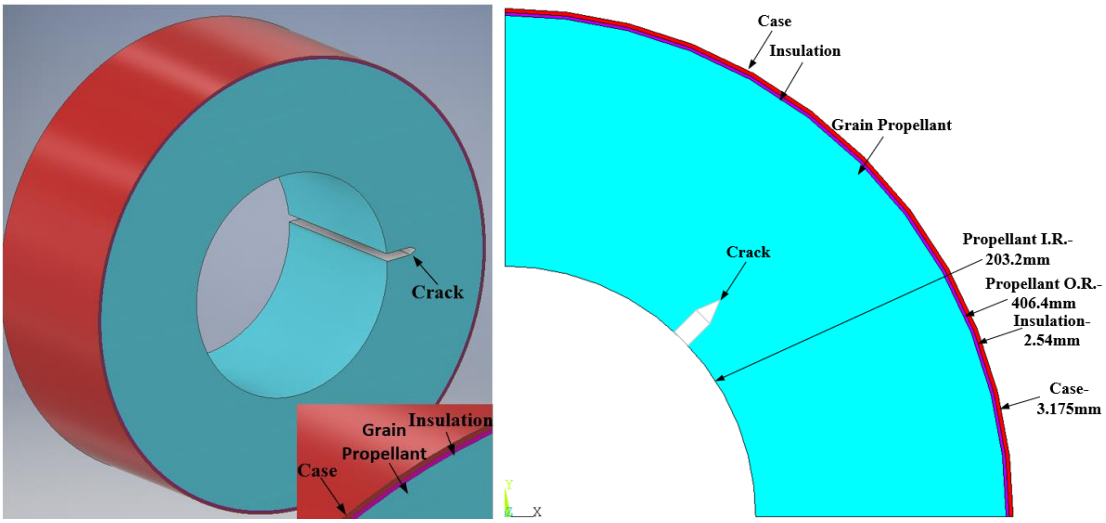

Figure 5: 3D Structure of propellant, insulation case and crack and one quarter of the cylinder with dimensions.

The linear elastic material properties of the case, insulation and grain propellant of SRM is shown in Table 2 bellow. Young's Modulus of grain propellant and insulation is depended on temperature but in this case, it was used theirs mean value.

Table 2: Material Properties

Material			
Parameter	**Grain propellant**	**Insulation**	**Case**
Poisson's ratio	0.499	0.499	0.3
Thermal Expansion Coefficient [strain / °C]	9.56e-5	8.75e-5	2.16e-6
Young Modulus	14.2 MPa	37.9 MPa	55.9 GPa

b. Finite Element Modeling

The model is constructed in ANSYS Mechanical APDL. All the cases are modeled to simulate the SRM cooling from 71°C to storage temperature -51°C. So, the total temperature drop is 120°C. In this model, on the left line of the cylinder it was constrained the horizontal displacement (displacement on X-axis) and on the bottom line it was constrained the vertical displacement (displacement on Y-axis). All the fixed lines are shown on the bellow figure.

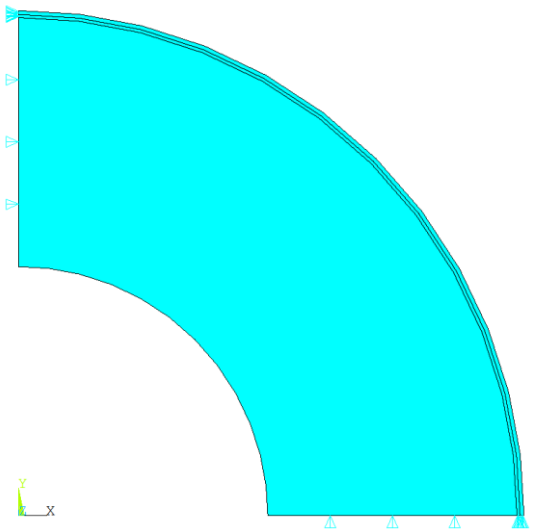

Figure 6: Fixed lines on the cylinder.

This model is meshed into more than 19000 8-node quadrilateral elements of plain strain and the mesh near the crack region is meshed more finely, as shown on Figure 8. After a lot of consideration and assessment of results it was selected 8-node over 4-node elements, because less elements provided the same accuracy on results, as shown in figure 6 and 7, where there are plotted the hoop strains of a specific crack length for different element types (4-node and 8-node) and density on the case and it is clearly that the 4-node elements results converge into 8-node elements results.

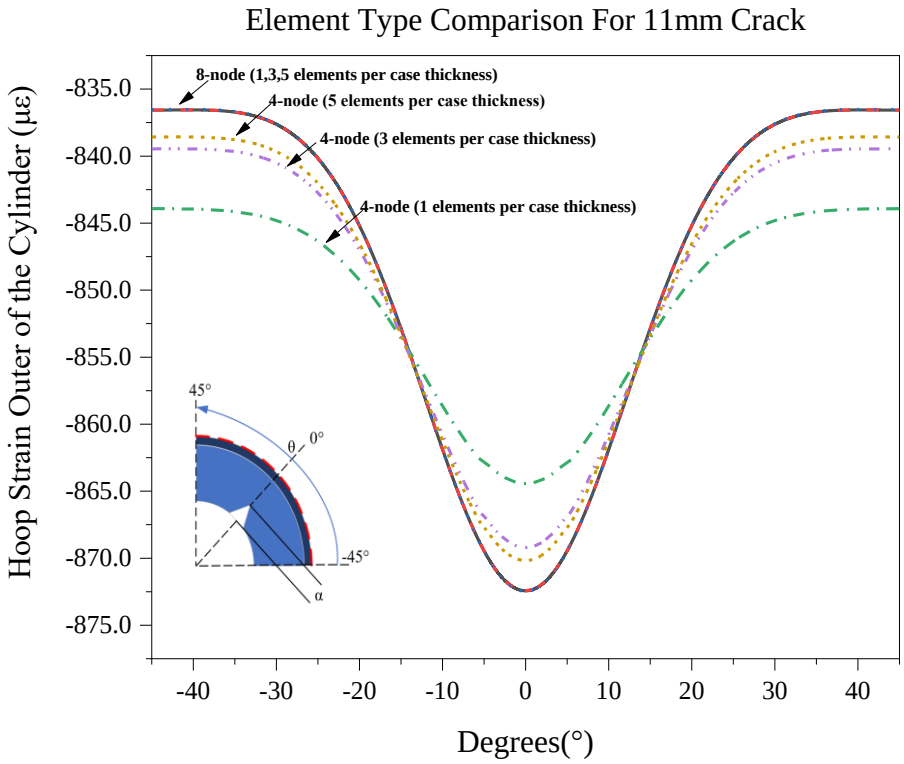

Figure 7: Comparison of different element types for grain propellant crack equal to 11mm.

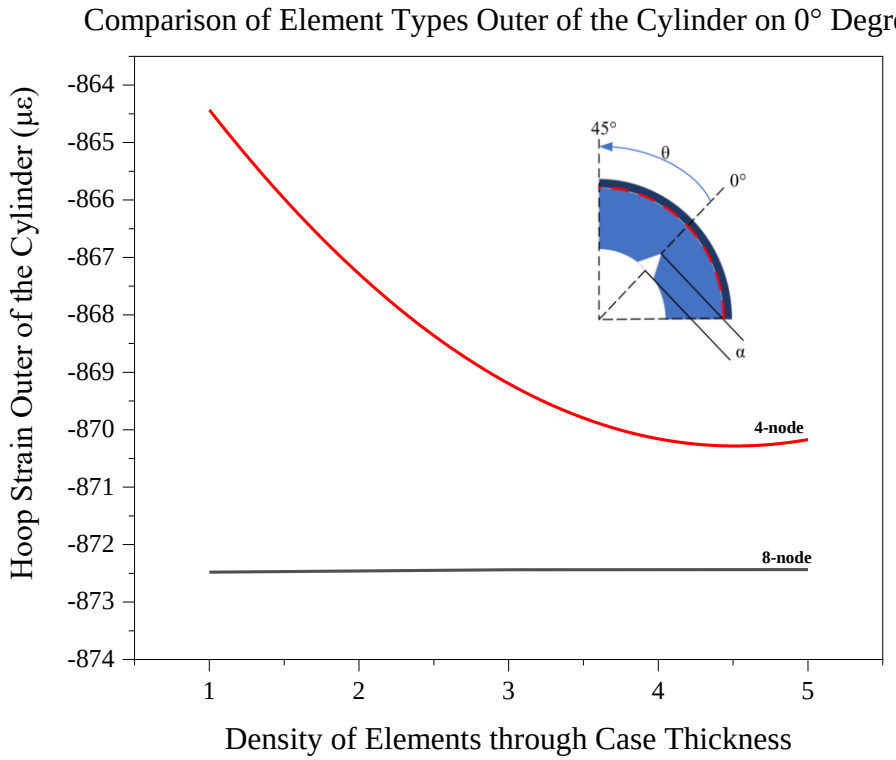

Figure 8: Comparison of different element types on the outer of the cylinder 0° degrees for grain propellant crack equal to 11mm.

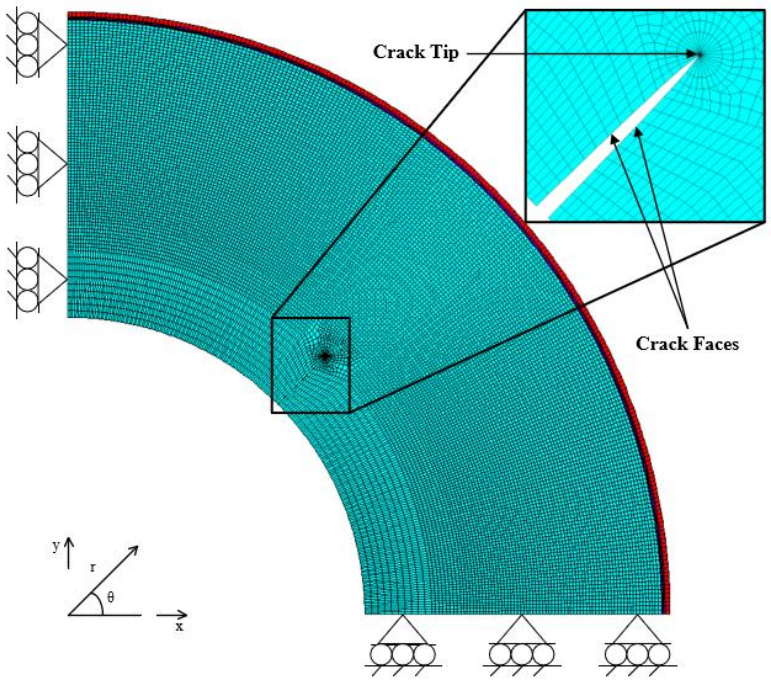

Figure 9: Mesh Design and corresponding boundary conditions.

On the current analysis except the 120°C temperature drop, it was designed a crack in the inner arc of the cylinder on 45º degrees to simulate the cracks that occur in SRMs. The list of the crack lengths (a-crack length) that have been analyzed is:

[2mm,7mm,8mm,10mm,11mm,16.1mm,21.5mm,26mm,31mm,35.9mm,40.9mm,45.8mm]

The selection of the crack lengths is completely random and it is based on bibliography.[16]

The design of the crack and its mesh [17] in the model is shown in Figure 9. This mesh refinement around the crack tip is a typical FE modeling strategy for calculating fracture mechanics related magnitudes, such as stress intensity factor (SIF) or Strain Energy Release Rate (SERR) for the purposes of static or fatigue crack growth simulations. Although such approaches are beyond the scope of this work, mesh refinement was adopted here for ensuring that a smooth strain redistribution will be captured remotely.

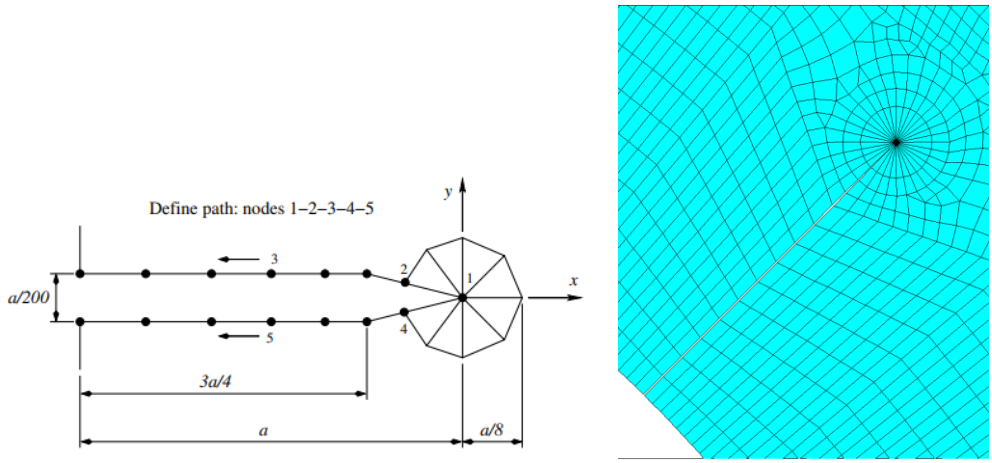

Figure 10: Crack Design and mesh near the crack tip.

c. ANN as a Surrogate Model

For training the ANN, firstly, it has been considered an uncertainty on the material properties and specific ±5% for young modulus and ±10% for thermal coefficient and in that way a matrix 6×1000 has been made for the material properties. Then, importing this matrix into ANSYS and shuffling the rows the program ran for 1000 different cases. With these results a neural network for regression has been trained, which performance can be seen in the following figures.

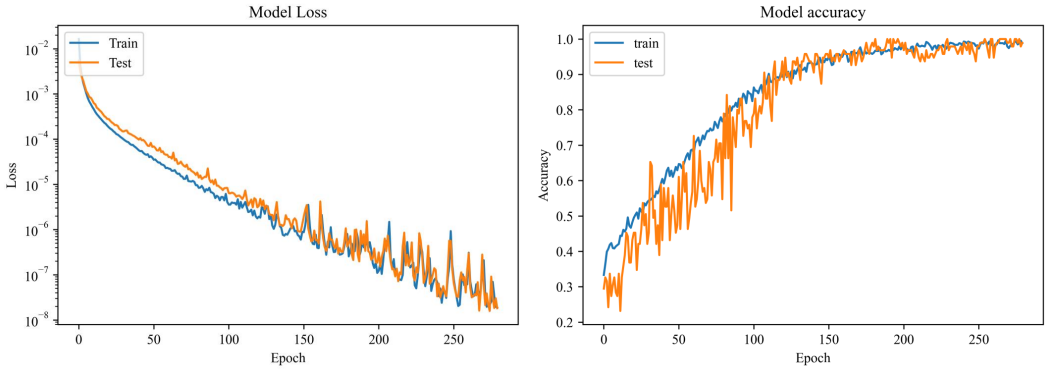

Figure 11: Performance of ANN.

It is clearly that the loss of the neural network is very low and the accuracy is very close to 1. Then this model has been used to propagate these results for 100.000 different cases of material properties. This processed has been followed both for the healthy and damaged model.

IV. Signal Exploration – Feature Engineering

First of all, it was important to understand the stress and strain patterns on the undamaged model and then on the model with the crack. Through the figures 11 to 14 there are presented the contour plots of hoop strain-stress and radial strain-stress for each model. The crack length of 11mm is selected randomly here. Further in the analysis there are analyzed more crack lengths.

As it is shown in figure 11a&b, it is clearly that both hoop and radial strains are bigger in the inside arc of the grain propellant and they are gradually reduced to the outer arc of the cylinder for the model with no crack. Tha maximum value of hoop strain is 0.048486 and of the radial strain is -0.057814.

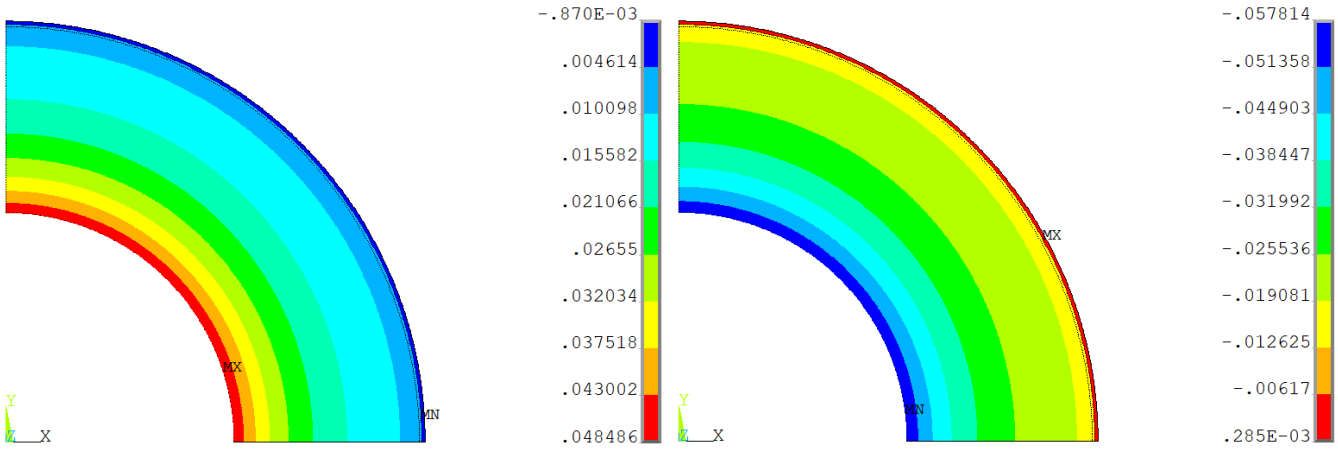

Figure 12a&b: Undamaged Model a. Hoop Strain b. Radial Strain.

Also, for the undamaged model, hoop stresses are smaller in the inside arc and bigger in the outer arc but the radial stresses are smaller on the inside of the cylinder and they are gradually increased to the case where the stress measurements due to different material are again smaller and are gradually reduced to the outer of the cylinder, as shown in figure 12a&b.

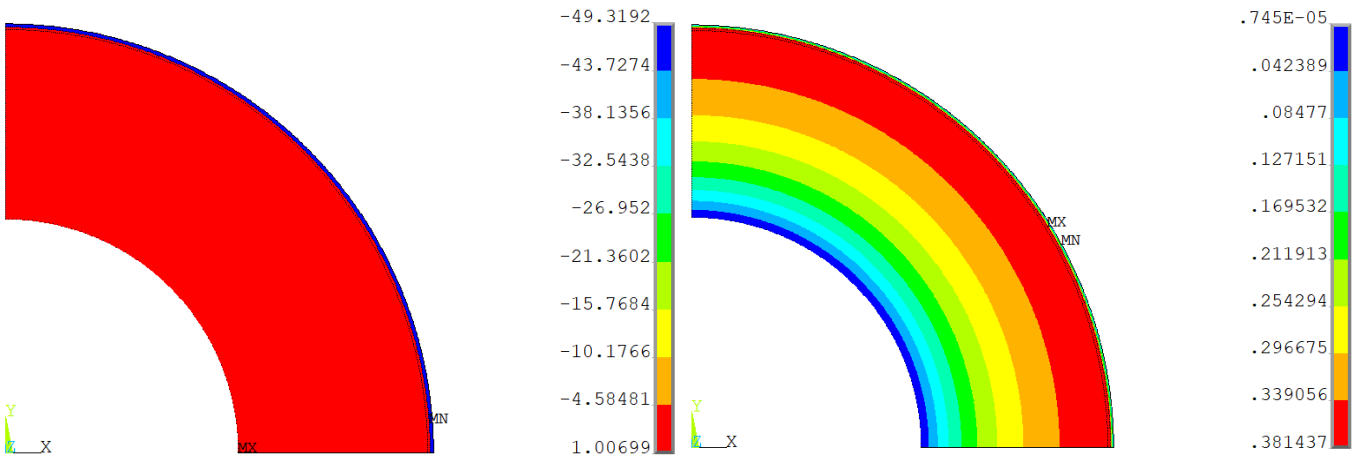

Figure 13a&b: Undamaged Model a. Hoop Stress b. Radial Stress.

Respectively, as it shown in figure 13a&b, hoop and radial strains are gradually reduced from the inside to outer of the cylinder but the maximum measurements are located near the crack tip. The maximum value of hoop strain is 0.152771 and of radial strain is -0.159751.

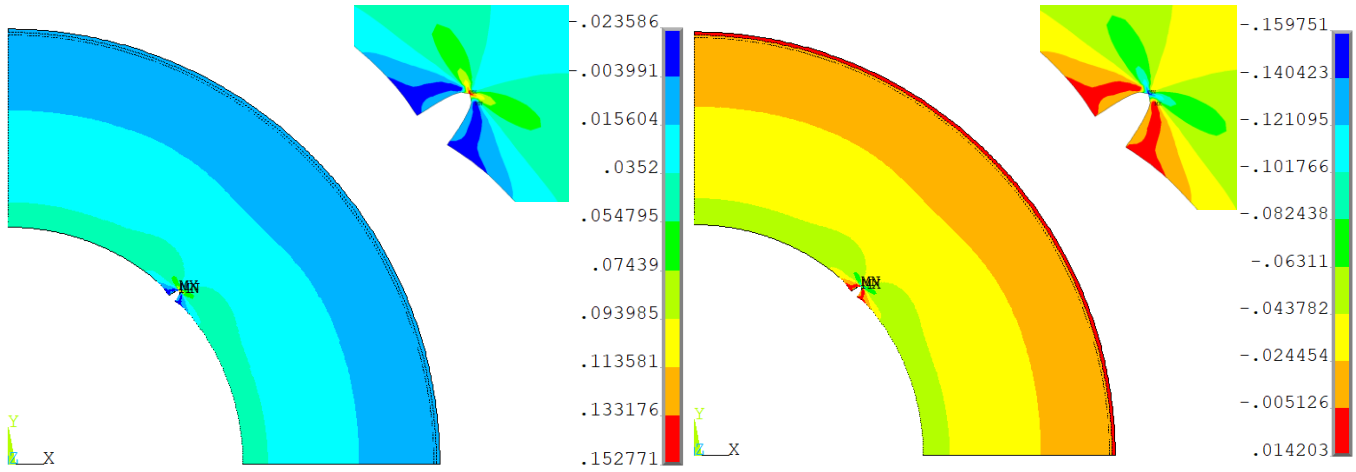

Figure 14a&b: Crack 11mm a. Hoop Strain b. Radial Strain with zoom on crack.

Furthermore, as shown in figure 14a&b, hoop and radial stresses are gradually increased from inside to outer of the cylinder but with the maximum measurements located at the crack tip.

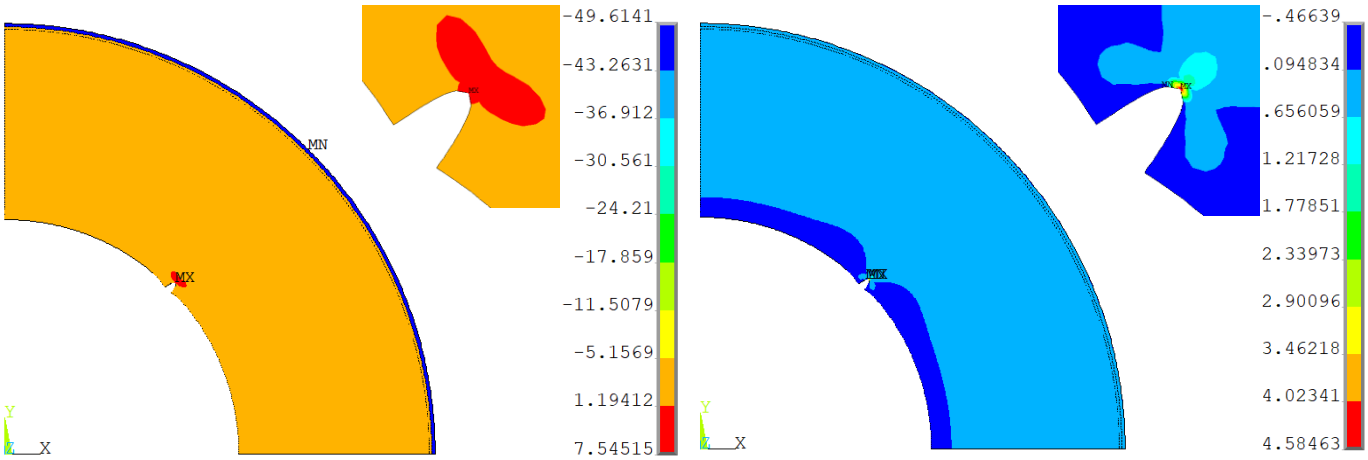

Figure 15a&b: Crack 11mm a. Hoop Stress b. Radial Stress.

The collected results are focused on the outer of the cylinder and on the middle of the insulation, and on the hoop strain and stress where the results measurements were significantly bigger, where it is possible to place sensors. As shown in figure 15, where there are plotted the residual strains on the outer of the cylinder (Damaged model strains-Healthy model strains) for different crack lengths on the hoop direction, it is easily observed that the bigger measurements are located away from the crack. Respectively, for middle of

insulation, it is observed that strains are significant smaller on the sides and bigger on the crack tip, which can be seen in figure 16.

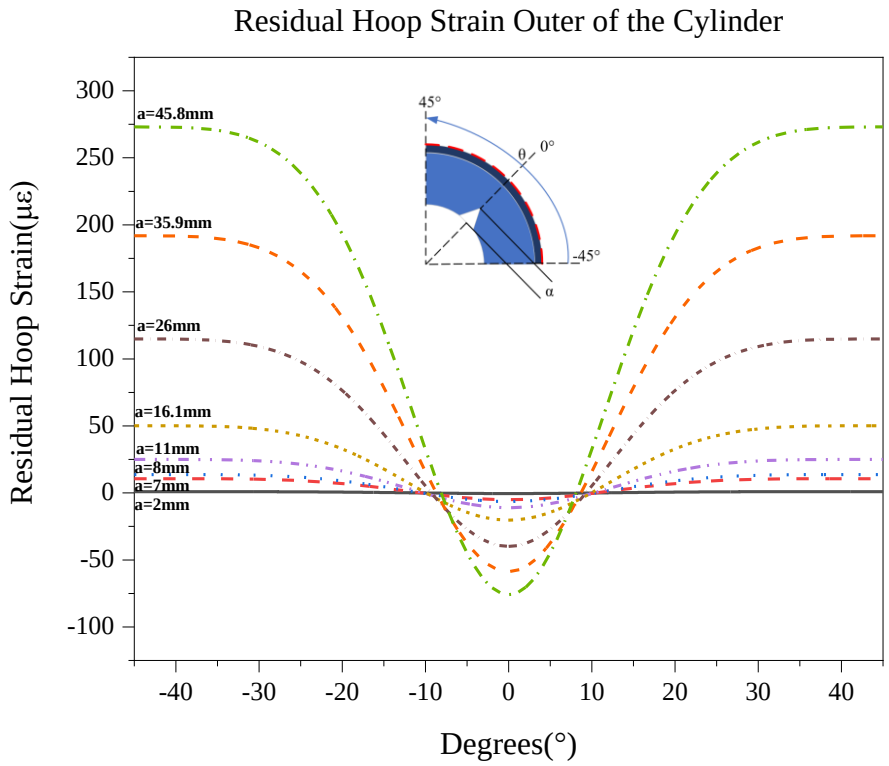

Figure 16: Residual Hoop Strain Outer of the Cylinder for Different Crack Lengths.

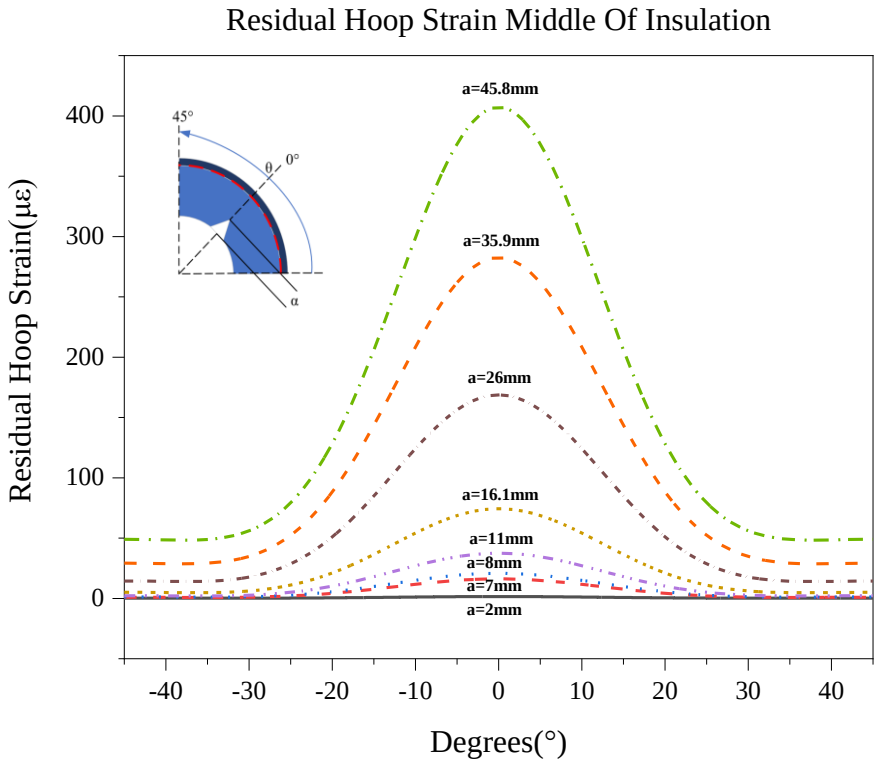

Figure 17: Residual Hoop Strain Middle of Insulation for Different Crack Lengths.

Respectively for residual hoop stress in figure 17 and 18 there are plotted the hoop stresses for outer of the cylinder and middle of insulation for different crack lengths.

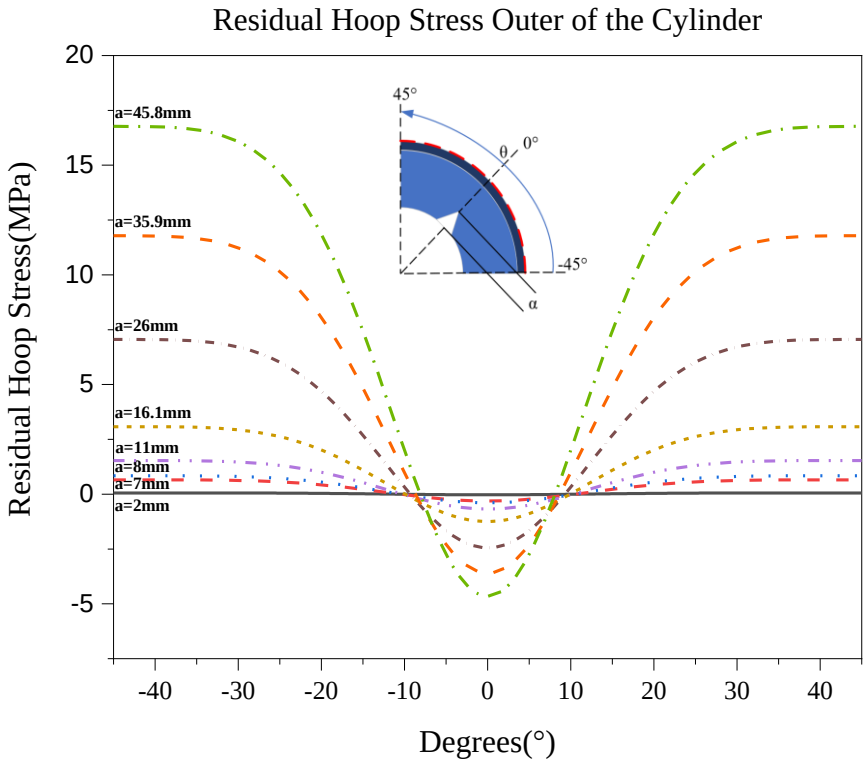

Figure 18: Residual Hoop Stress Outer of the Cylinder for Different Crack Lengths.

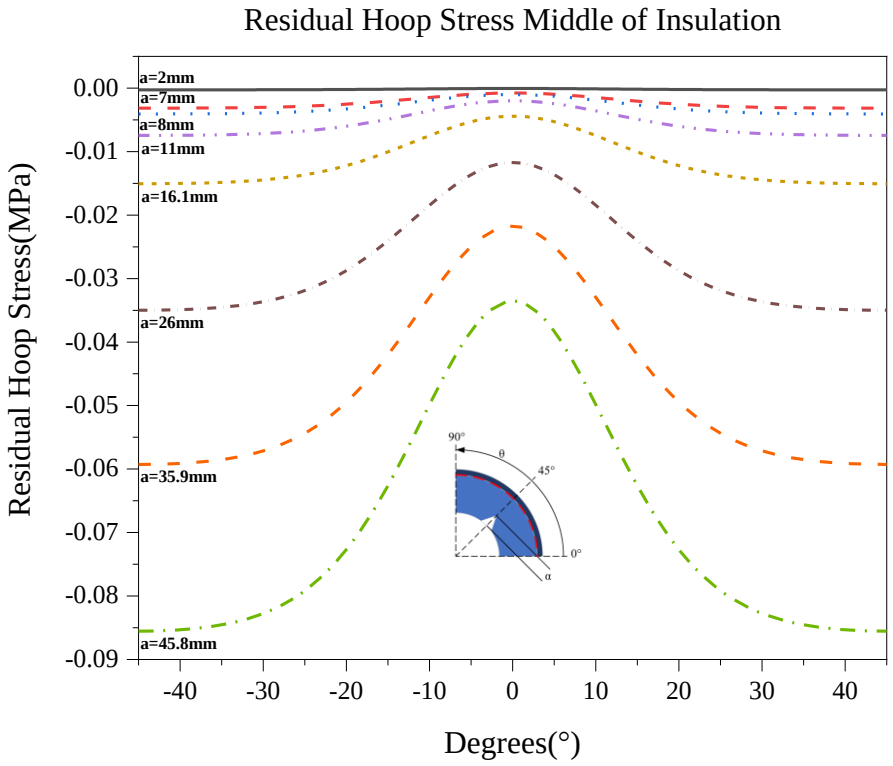

Figure 19: Residual Hoop Stress Middle of Insulation for Different Crack Lengths.

In this thesis, the main analysis is carried out for hoop strains on the outer of the cylinder and middle of the insulation, because it was taken into account that the sensors placed in the structure measure strain. In figures 19 and 23 are plotted the residual strain for different crack lengths and degrees starting from crack tip as 0º degree. These graphs are really helpful cause they show respectively the sensors location from crack tip what measures it really gets. Also, there are included graphs, figure 20 and 24, with zoom of the results of figures 19 and 23 so the results are more readable. The curves of these graphs are constructed with polynomial fits, as shown in figures 22 and 25, so the results for intermediate crack values are more accurate and the curves smoother. The method of the fitting will be discussed further in this thesis. From these graphs it is clearly, as written before, that placing a sensor on 45º degrees from the crack tip on the outer of the cylinder and on crack tip on middle of insulation gives better and more accurate measurements for the damaged situation.

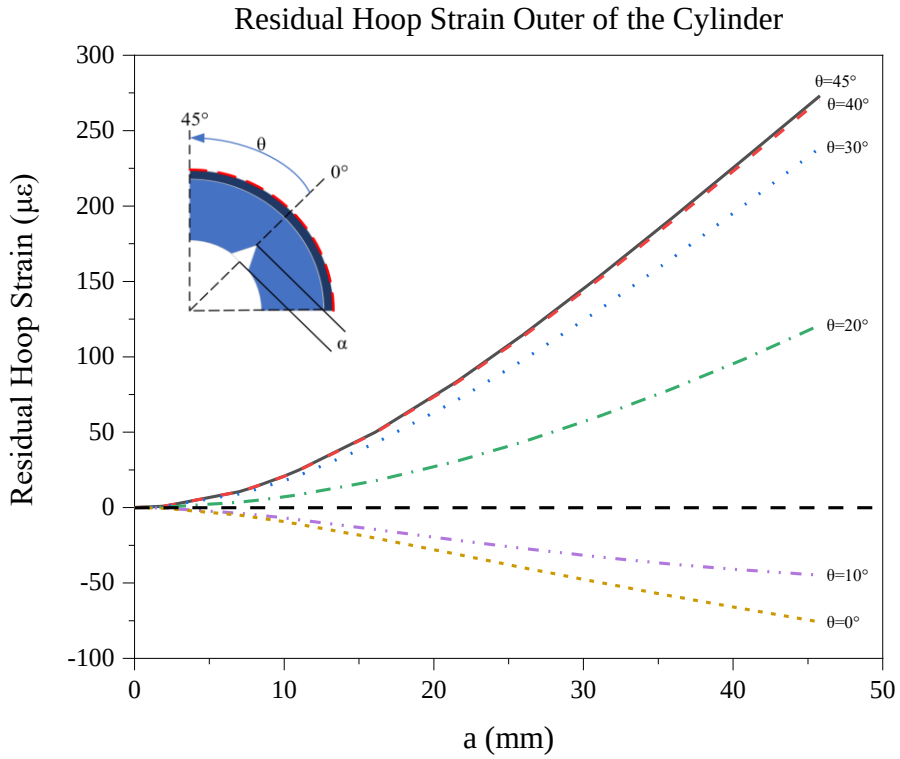

Figure 20: Residual Strains Outer of the Cylinder for different crack lengths and degrees.

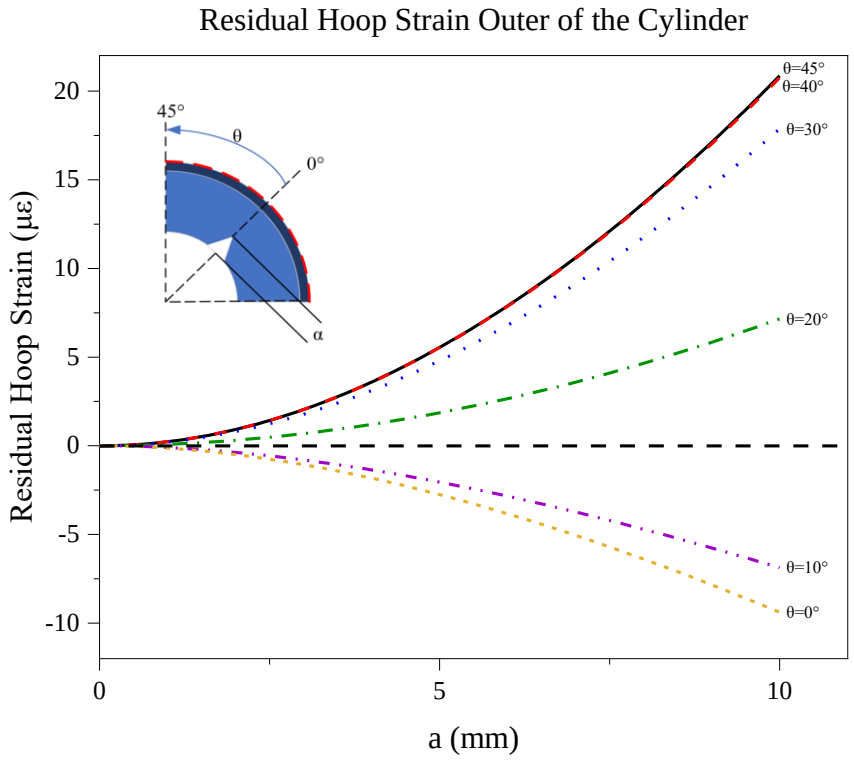

Figure 21: Residual Strains Outer of the Cylinder for different crack lengths and degrees Zoom for Crack Lengths 0-10mm.

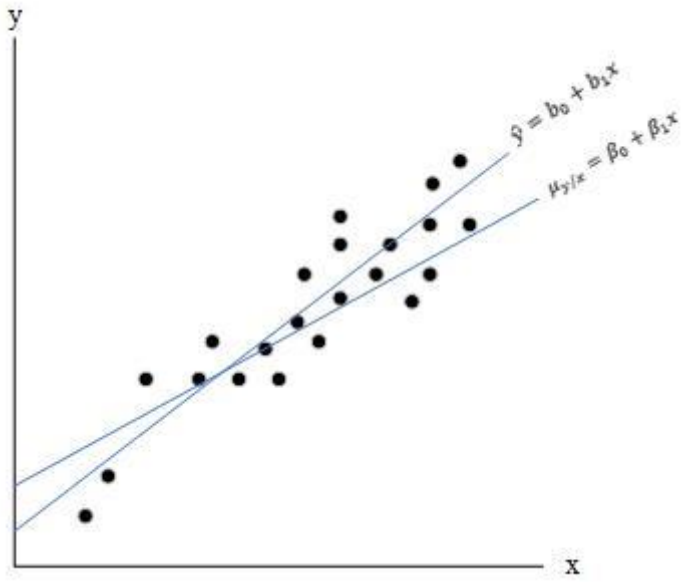

Figure 22: Scatter Diagram with Regression Lines.

Least square fitting is a mathematical procedure for finding the best-fitting curves to a given set of points by minimizing the sum of the squares of the offsets of the points from the curve [18]. In the method of Least Squares, we shall find b_0 and b_1, the estimates of β_0 and β_1, so that the sum of squares of the residuals is a minimum. All that is shown in the above figure 19, where the $\hat{y}$ line is the fitted regression line and the other is a hypothetical true regression line. The residual sum of squares is often called the sum of squares of the

errors about the regression line and is denoted by SSE. This minimization procedure for estimating the parameters is called the method of least squares. Hence, we shall find a and b so as to minimize:

$$SSE = \sum_{i=1}^{n} e_i^2 = \sum_{i=1}^{n} (y_i - \hat{y})^2 = \sum_{i=1}^{n} (y_i - b_0 - b_i x_i)^2 \quad (32)$$

Differentiating SSE with respect to find b_0 and b_1, we have:

$$\frac{\partial (SSE)}{\partial b_0} = -2\sum_{i=1}^{n} (y_i - b_0 - b_1 x_i), \quad \frac{\partial (SSE)}{\partial b_1} = -2\sum_{i=1}^{n} (y_i - b_0 - b_1 x_i), \quad (33)$$

Setting the partial derivatives equal to zero and rearranging the rems, we obtain the equations:

$$nb_0 + b_1 \sum_{i=1}^{n} x_i = \sum_{i=1}^{n} y_i, \quad b_0 \sum_{i=1}^{n} x_i + b_1 \sum_{i=1}^{n} x_i^2 = \sum_{i=1}^{n} x_i y_i \qquad (34),$$

Which may be solved simultaneously to yield computing formulas for b_0 and b_1.

Given the sample $\{(x_i, y_i);\ i=1,2,...,n\}$, the least squares estimate b_0 and b_1 of the regression coefficients β_0 and β_1 are computed from the formulas:

$$b_1 = \frac{n\sum_{i=1}^{n} x_i y_i - (\sum_{i=1}^{n} x_i)(\sum_{i=1}^{n} y_i)}{n\sum_{i=1}^{n} x_i^2 - (\sum_{i=1}^{n} x_i)^2} = \frac{\sum_{i=1}^{n} (x_i - \bar{x})(y_i - \bar{y})}{\sum_{i=1}^{n} (x_i - \bar{x})^2} \text{ and}$$
$$b_1 = \frac{\sum_{i=1}^{n} y_i - b_1 \sum_{i=1}^{n} x_i}{n} = \bar{y} - b_1 \bar{x} \qquad (35)$$

R-squared (R^2) is a statistical measure that represents the proportion of the variance for a dependent variable that is explained by an independent variable or variable in a regression model. R-squared explains to what extent the variance of one variable explains the variance of the second variable [19]. The R-Squared is given by the equation:

$$R^2 = 1 - \frac{SSE}{SST}, \ where:$$
$$SST = \sum_{i=1}^{n} (y_i - \bar{y}_i)^2 \qquad (36)$$

Where, SST is the total corrected sum of squares.

The Adjusted R-Squared is a modified version of R-Squared that has been adjusted for the number of predictors in the model. The adjusted R-squared increases when the new term improves the model more than would be expected by chance. It decreases when a predictor improves the model by less than expected.

Typically, the adjusted R-squared is positive, not negative. It is always lower than the R-squared. It is given by formula:

$$R^2_{adj} = 1 - \frac{SSE/(n-k-1)}{SST/(n-1)}, (37)$$

Where n is the number of points in the data sample and k is the number of independent regressors.

Table 3: Least Square Fitting for Outer of the Cylinder.

Equation	**Y=Intercept+B1*x^1+B2*x^2+B3*x^3+B4*x^4+B5*x^5**					
	Residual Hoop Strain Outer of the Cylinder					
Plot	**θ=45°**	**θ=40°**	**θ=30°**	**θ=20°**	**θ=10°**	**θ=0°**
Intercept	-4.74193e-4	-0.00207	-0.00565	-0.00296	0.01029	0.01335
B1	-0.00165	0.00182	0.01074	0.00878	-0.01594	-0.02213
B2	0.23617	0.23579	0.20301	0.07532	-0.09272	-0.12275
B3	-0.00285	-0.003	-0.00274	-4.86532e-4	0.00292	0.00355
B4	1.15239e-5	1.57931e-5	2.11077e-5	2.66918e-6	-3.92067e-5	-4.76858e-5
B5	3.05289e-9	-2.86437e-8	-8.55254e-8	-1.18829e-8	2.08772e-7	2.53658e-7
Residual Sum of Squares	1.47244e-5	2.40332e-5	2.12823e-4	6.68151e-5	7.55964e-4	0.00128
R-Squared	1	1	1	1	1	1
Adj. R-Square	1	1	1	1	1	1

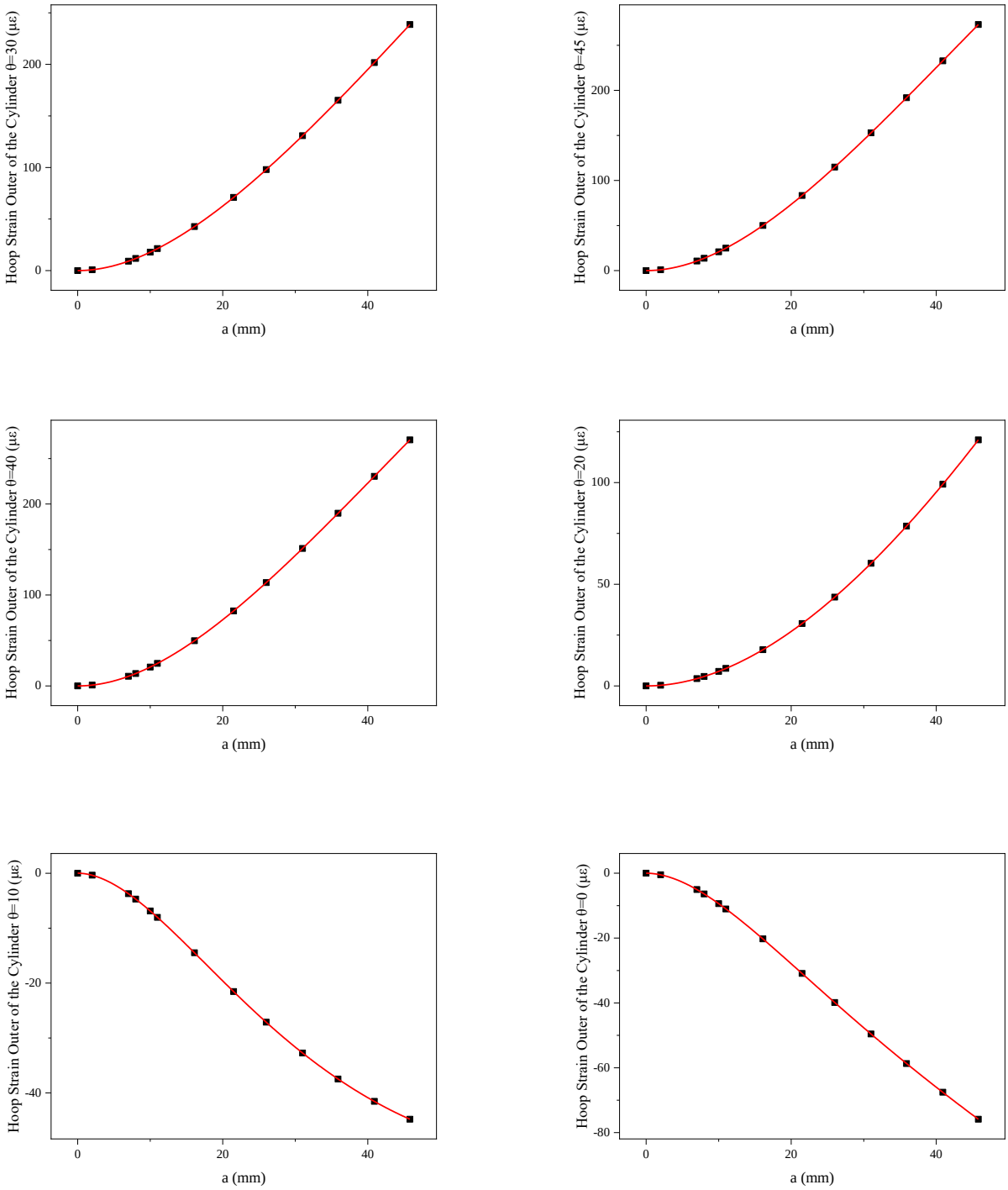

Figure 23: Polynomial Fitting of Figure 20 Curves.

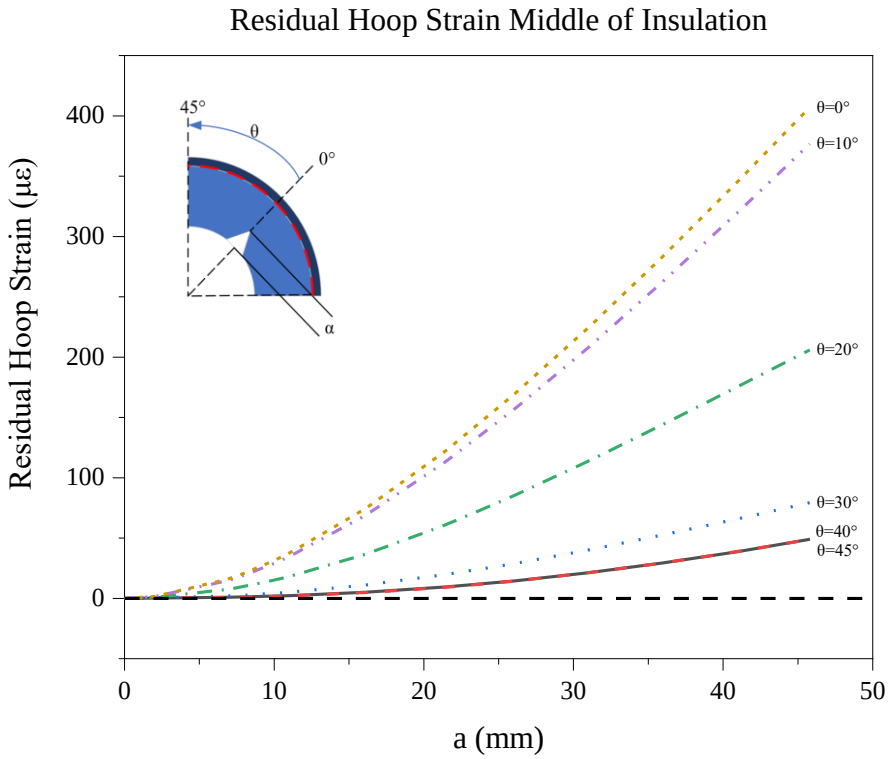

Figure 24: Residual Strains Middle of the Insulation for different crack lengths and degrees.

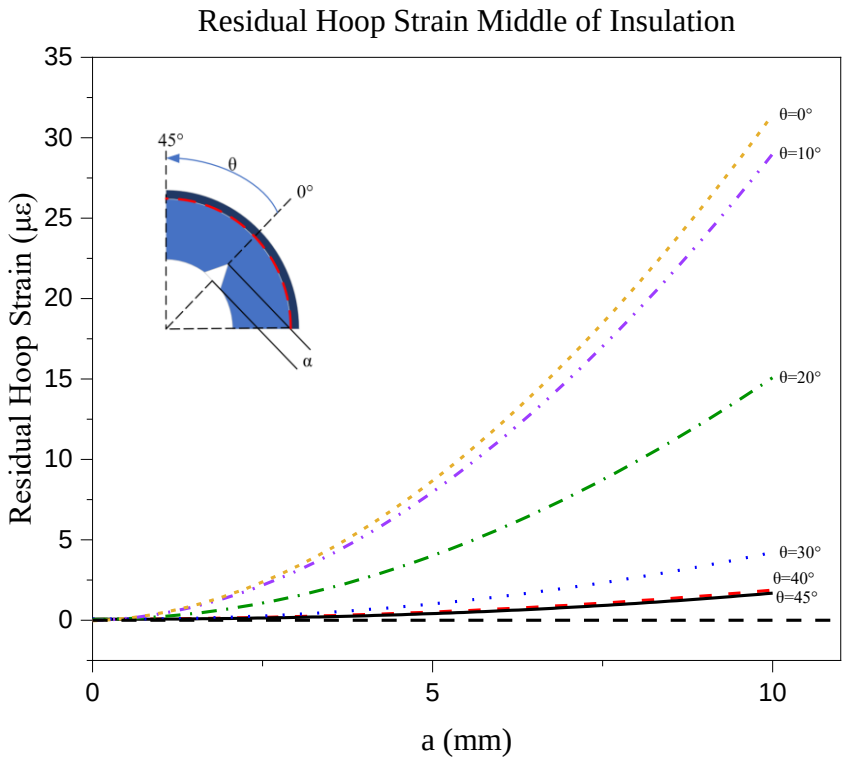

Figure 25: Residual Strains Middle of the Insulation for different crack lengths and degrees Zoom for Crack Lengths 0-10mm.

Table 4: Least Square Fitting for Middle of Insulation.

Equation	Y=Intercept+B1*x^1+B2*x^2+B3*x^3+B4*x^4+B5*x^5					
	Residual Hoop Strain Middle of Insulation					
Plot	**θ=45°**	**θ=40°**	**θ=30°**	**θ=20°**	**θ=10°**	**θ=0°**
Intercept	-0.02928	-0.01654	0.05597	0.08304	0.05931	0.04555
B1	0.13409	0.11014	-0.00153	-0.0378	-5.4723e-4	0.01999
B2	0.34298	0.31731	0.16727	0.04465	0.01206	0.01268
B3	-0.00441	-0.00402	-0.00173	9.14996e-5	4.76353e-4	4.00383e-4
B4	2.39271e-5	2.09479e-5	4.79297e-6	-4.88172e-6	-5.04649e-6	-3.86972e-6
Residual Sum of Squares	0.02401	0.01415	0.01228	0.03309	0.01454	0.00764
R-Squared	1	1	1	1	1	1
Adj. R-Square	1	0.99999	0.99999	1	1	1

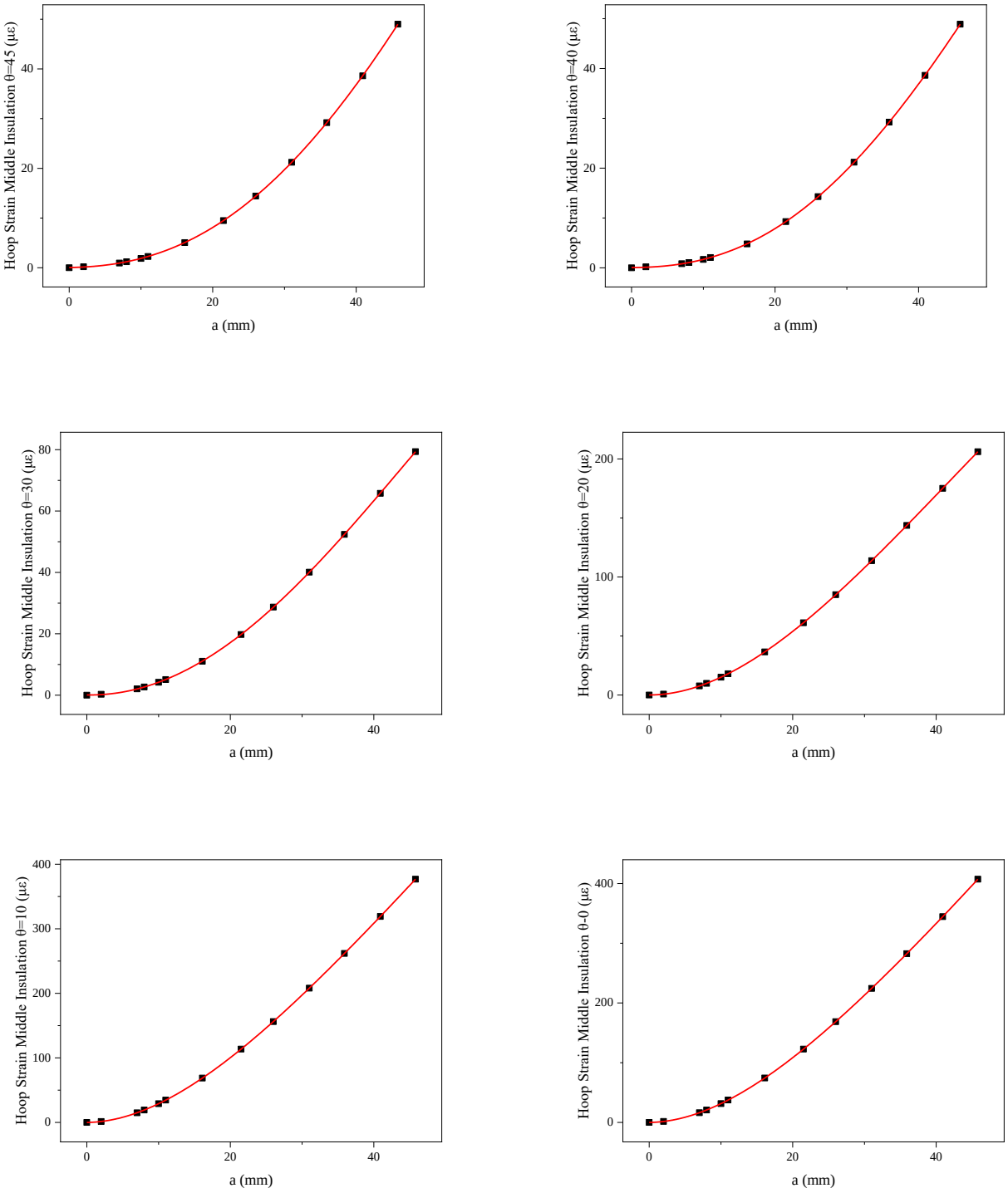

Figure 26: Polynomial Fitting of Figure 23 Curves.

V. Deterministic Signal in Noise

Using the theory described in II c. Detection Theory, the detection problem is mean-shifted. At 0 mm crack length we have white Gaussian noise with zero mean and σ=5με standard deviation. Then, for every crack length is taken a strain gaussian distribution with Δε mean and σ=5με standard deviation. Null hypothesis is continuously the noise only gaussian distribution and alternative hypothesis is the signal associated with each crack strain distribution.

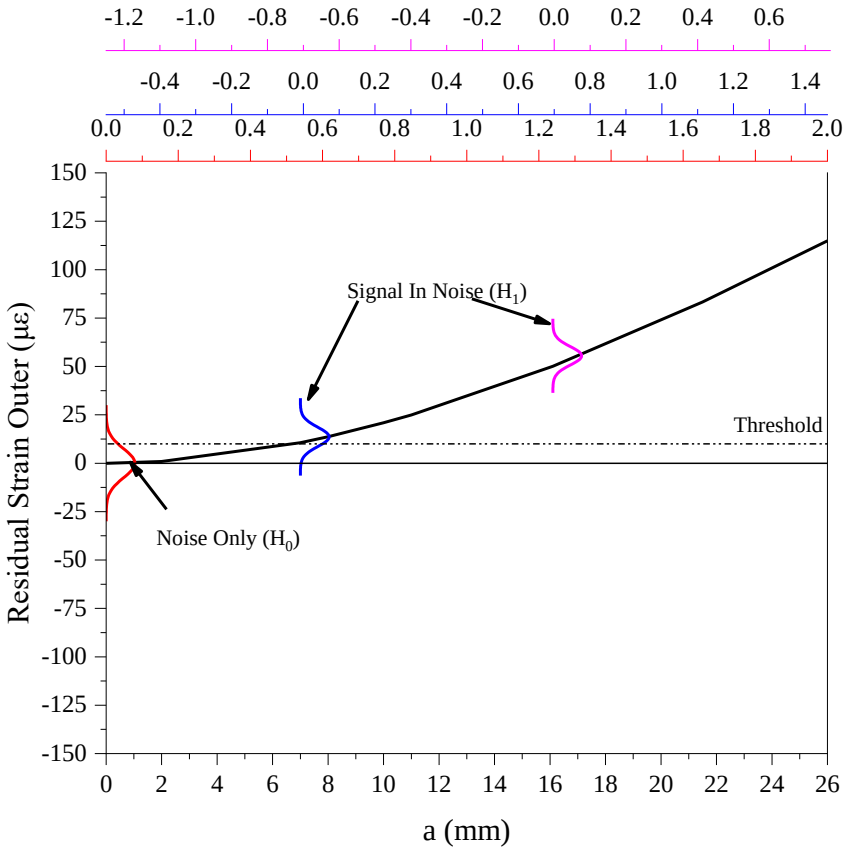

Figure 27: Gaussian Distribution of Residual Strain.

Using now the (17) equation for a predefined P_{FA} and Δε results that have been analyzed previously we want to find probability of detection. Based on the results of the constructed Python code, which are shown in Figure 27, we can see for different P_{FA} from what crack length we can detect that the structure is damaged for $P_D = 99.9\%$.

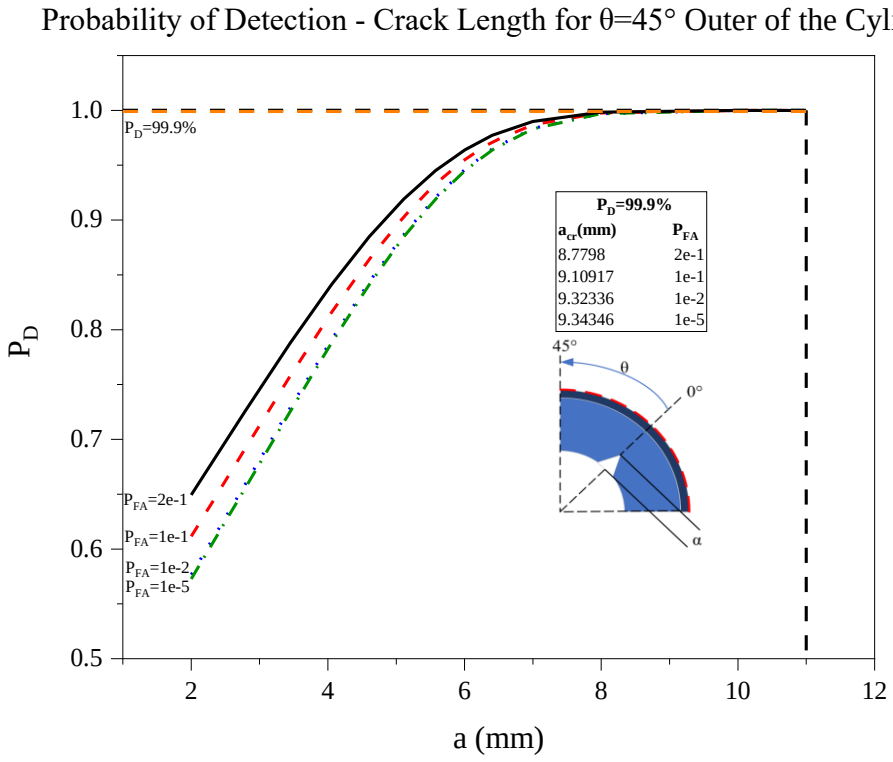

Figure 28: Probability of detection-Crack Length-Probability of false alarm Outer of the Cylinder θ=45°.

Also, as it is shown in Figure 28, if we place a sensor in 0 or 10 degrees, we increase the detector's resolution because we identify smaller cracks with the same accuracy.

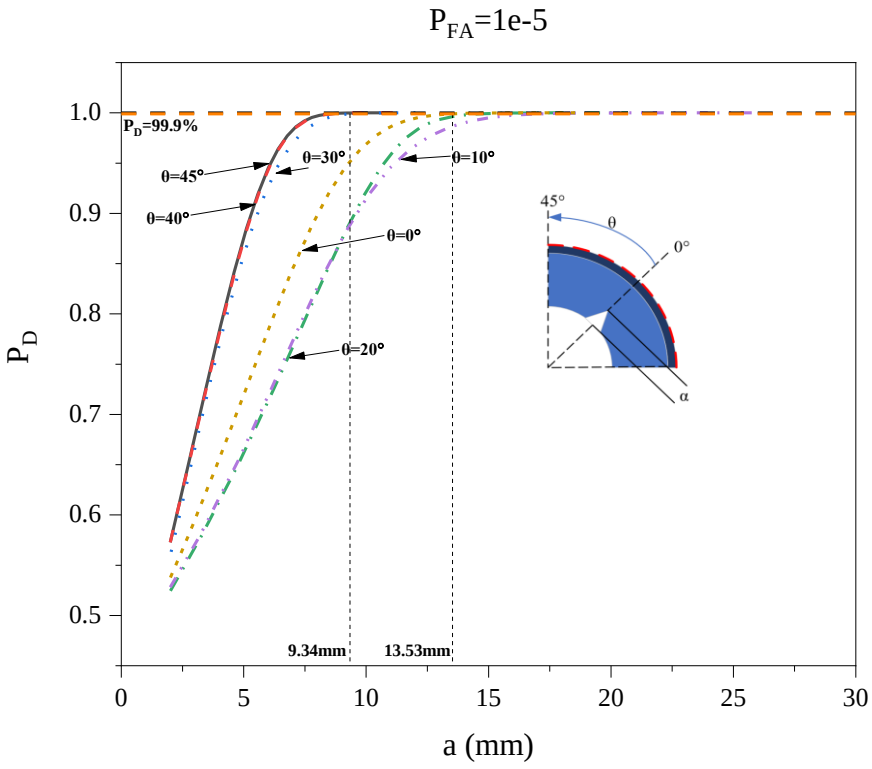

Figure 29: Probability of detection-Crack Length-Probability of false alarm-Degrees Outer of the Cylinder.

Respectively, for the middle of the insulation we can see in Figure 29 for what crack lengths we get probability of detection 99.9%. Furthermore, as shown in Figure 30, placing a sensor in 45 degrees is more efficient than on the sides because we will get damage results for smaller crack lengths.

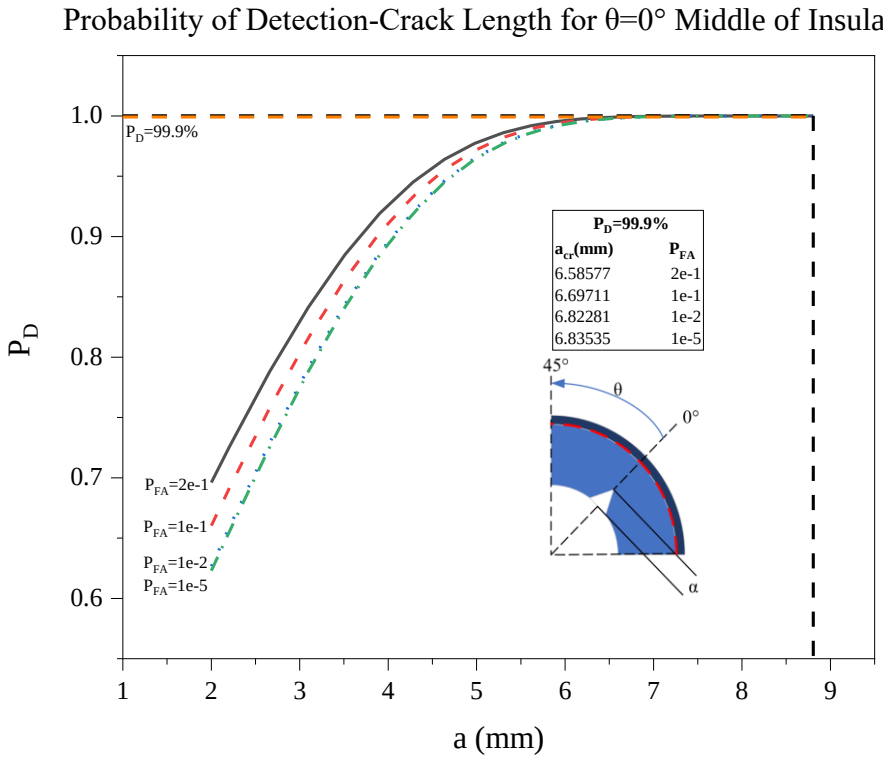

Figure 30: Probability of detection-Crack Length-Probability of false alarm Middle of Insulation for θ=45°.

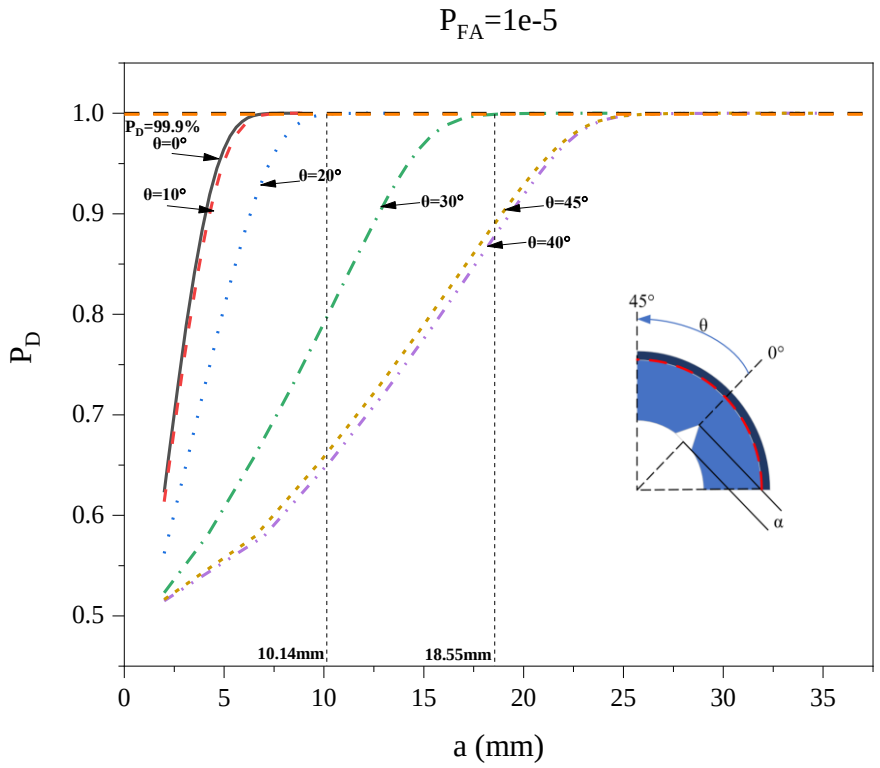

Figure 31: Probability of detection-Crack Length-Probability of false alarm-Degrees Middle of Insulation.

Another way of summarizing the detection performance of a NP detector is to plot P_D versus P_{FA}. Every curve of this diagram is constructed for a standard mean value Δε(a). As expected, the performance is higher for big P_{FA} and is decreased for lower P_{FA}.

The ROC curves in Figures 31 and 32 summarize the performance of a single sensor placed either on the case or in the insulation. The grey area (lower triangle) denotes a lack of information gain, and any inferences are purely speculative. These curves correspond to the optimal setting in the Neyman-Pearson detection theory, which can be used in a risk assessment analysis. We first define the possibility of false alarm and detection in our system, and then we determine the corresponding minimum crack length that is considered detectable given the defined performance metrics. It is shown that placing a sensor at 45° on the outer of the cylinder the detector detects a crack of approximately 10mm with a great performance. Respectively, when a sensor is being placed on 0° on the middle of the insulation a crack of approximately 8 mm is recognized with a great performance.

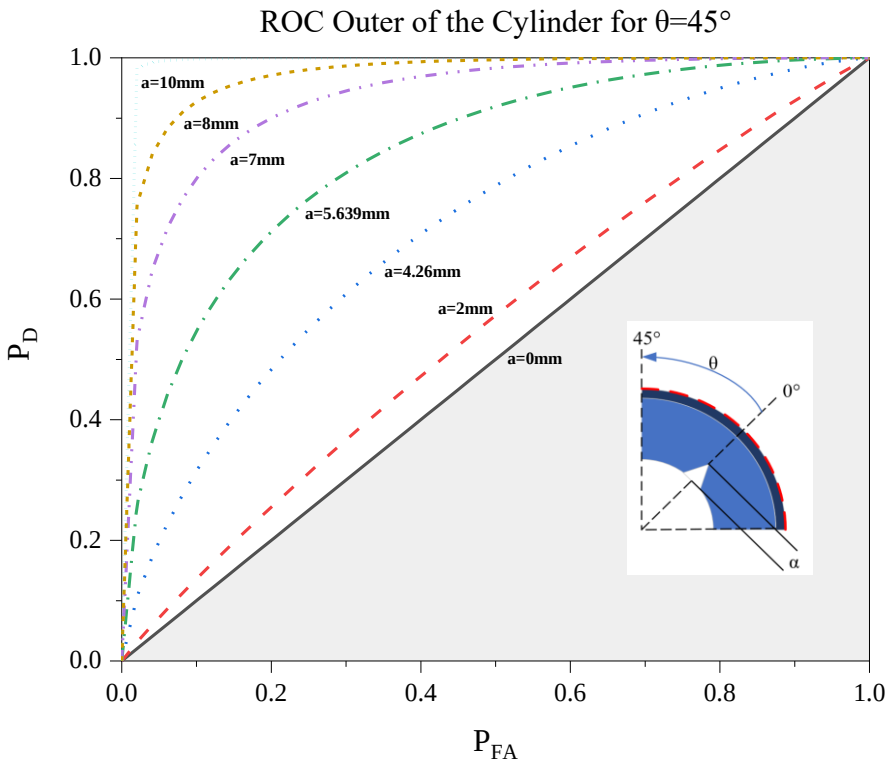

Figure 32: ROC Outer of the Cylinder for θ=45°.

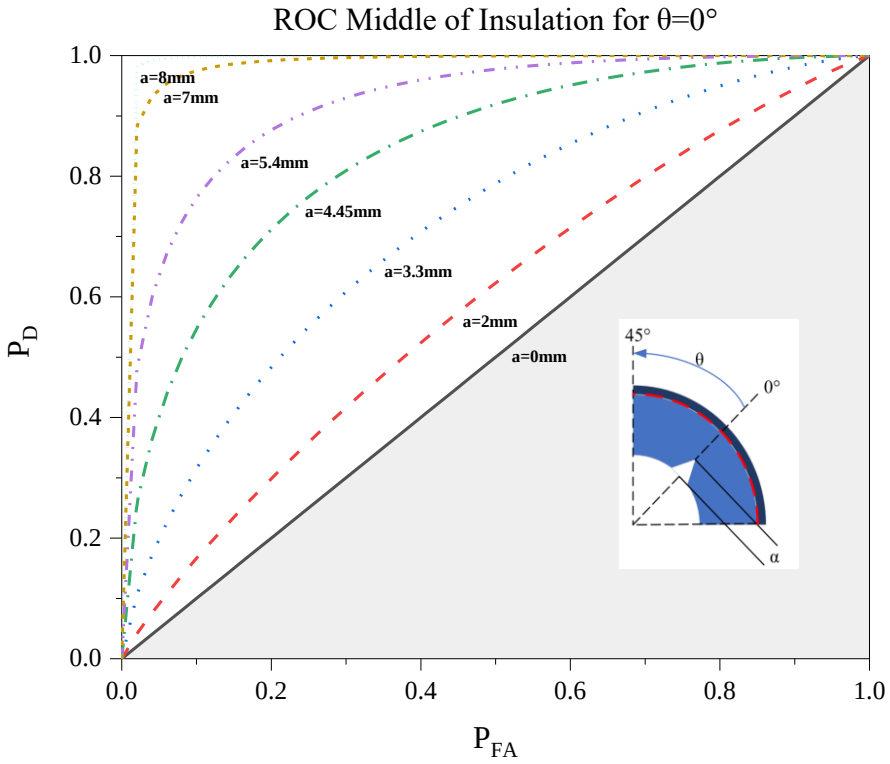

Figure 33: ROC Middle of the Insulation for θ=0°.

VI. Aleatoric Probabilistic Modeling

In this part, the first process that is done is the regression of the 1000 data sample from the Ansys program to the 100000-sample data. First, for the healthy model an artificial neural network has been used with the following characteristics:

First layer and first hidden layer: Dense=32, activator: relu

Second hidden layer: Dense=32, activator: relu

Test size= 5%

Validation size= 10%

Batch size=10

Epochs=280

The performance of this neural network is shown in the 3 following graphs where it is clear that the loss of it is very low and the accuracy is very close to 1. In figure 34, the upper line refers to prediction results of grain propellant the bellow one to insulation and the down one to case. The blue line completely overlaps the red one, fact that shows that the predictions with the real results are closely to the same.

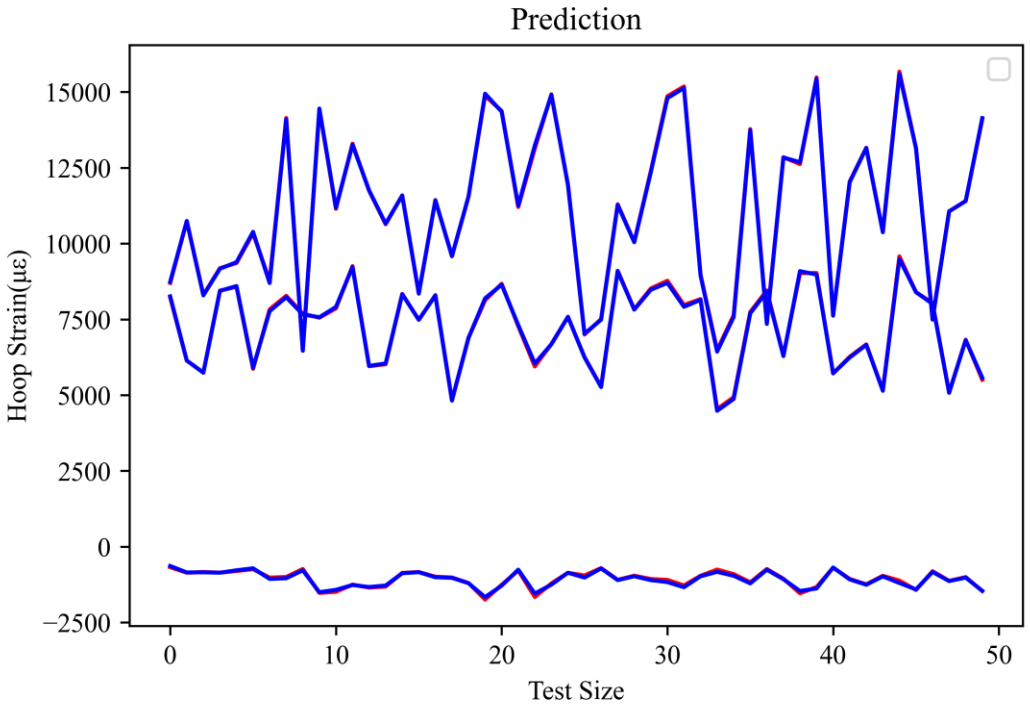

Figure 34: Prediction values versus actual values of the healthy model.

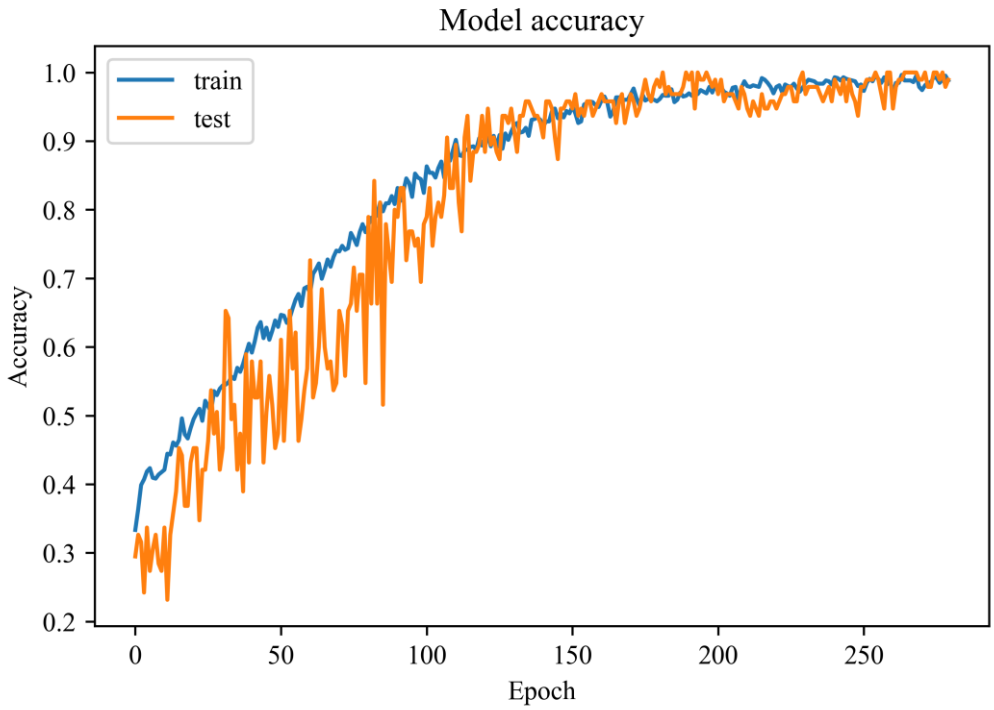

Figure 35: Accuracy of ANN for regression of the healthy model hoop strains.

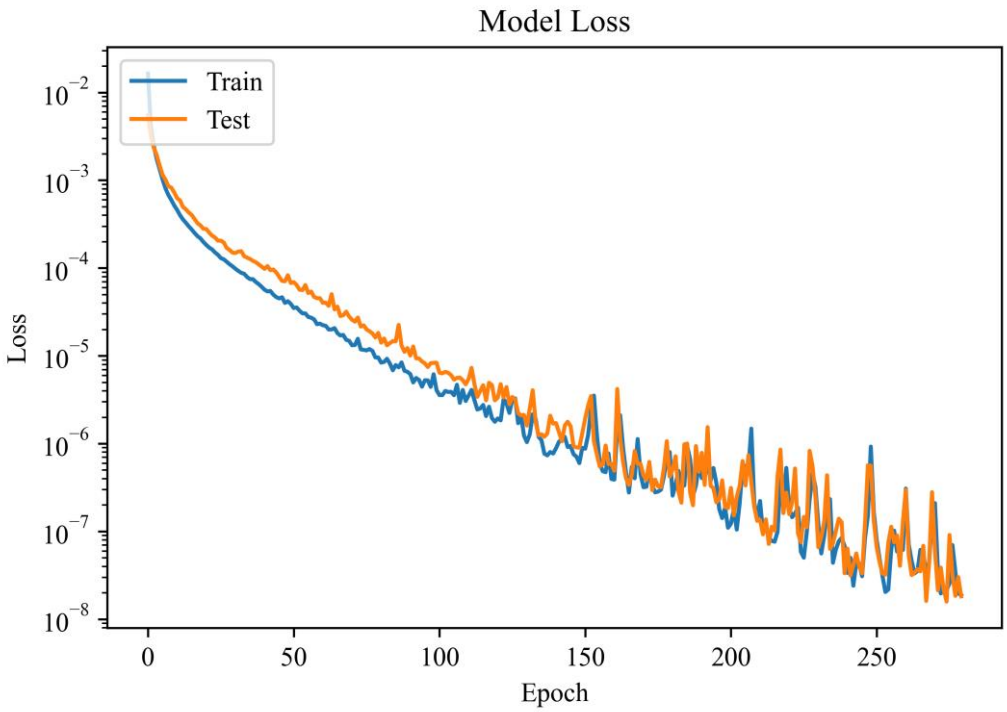

Figure 36: Loss of ANN for regression of the healthy model hoop strains.

Also, there are plotted the predicted hoop strains versus the hoop strains from the previous deterministic analysis, the hoop strain in noise, for the three different areas, grain propellant, insulation and case, where the analysis that is performed in this case is significantly larger than the previous one. For each area, there is

a q-q plot, which indicates that the data follows the normal distribution and a convergence plot which shows how the data converge into the mean value.

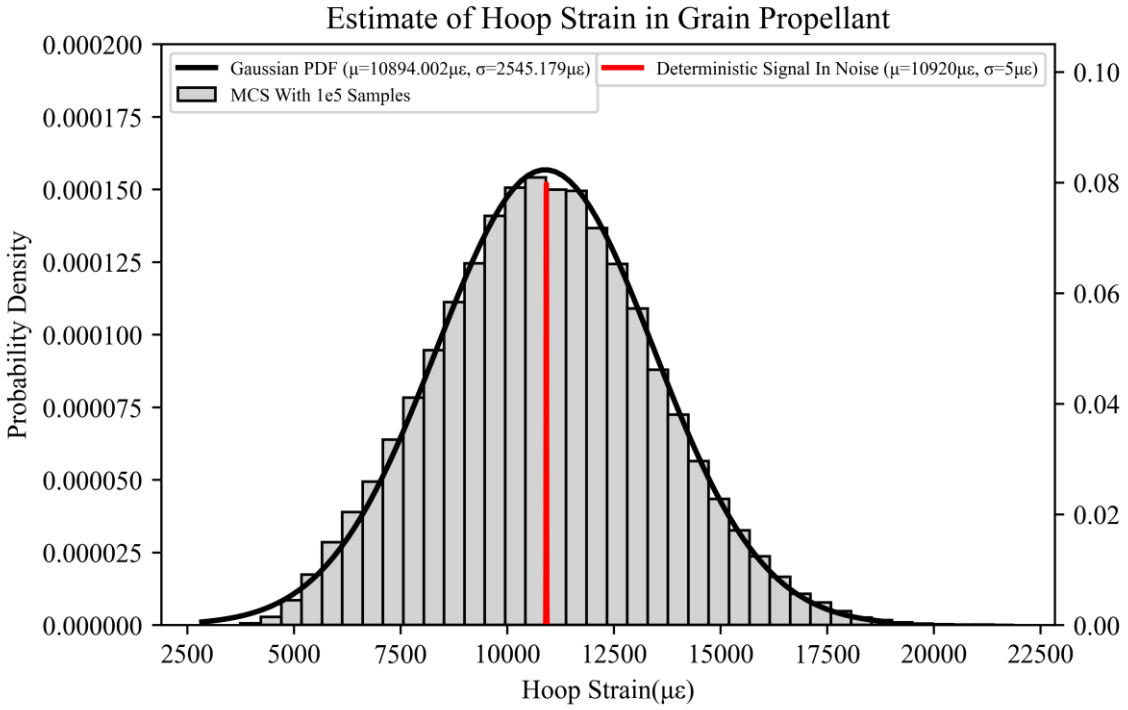

Figure 37: Predicted Hoop Strains distribution versus Deterministic Signal in Noise in Grain propellant.

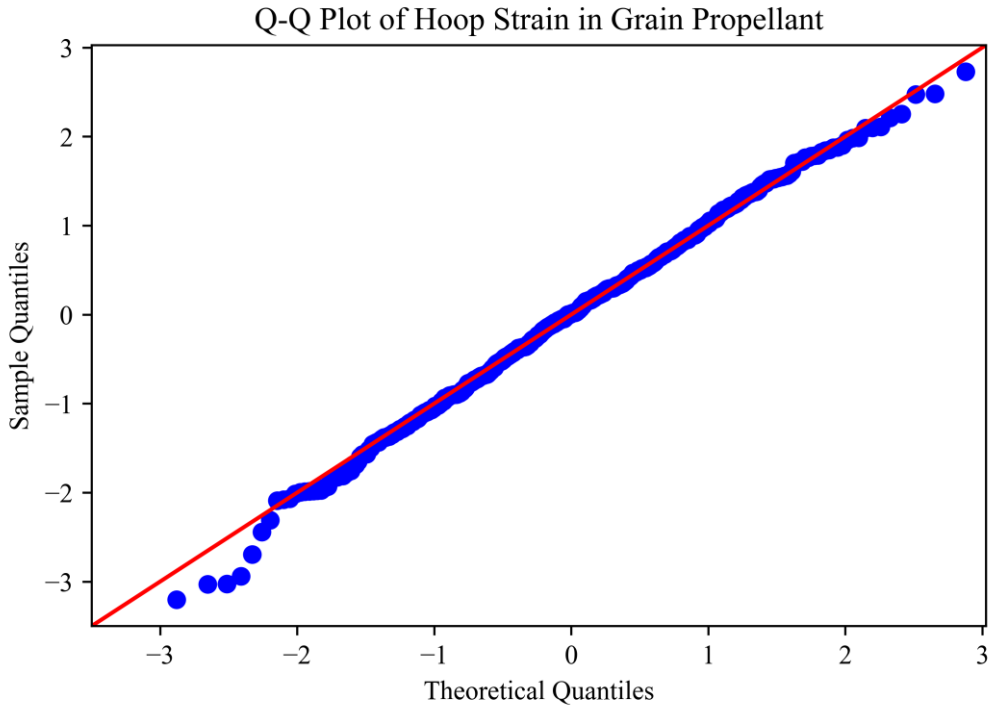

Figure 38: Q-Q plot of Predicted Hoop Strains in Grain propellant.

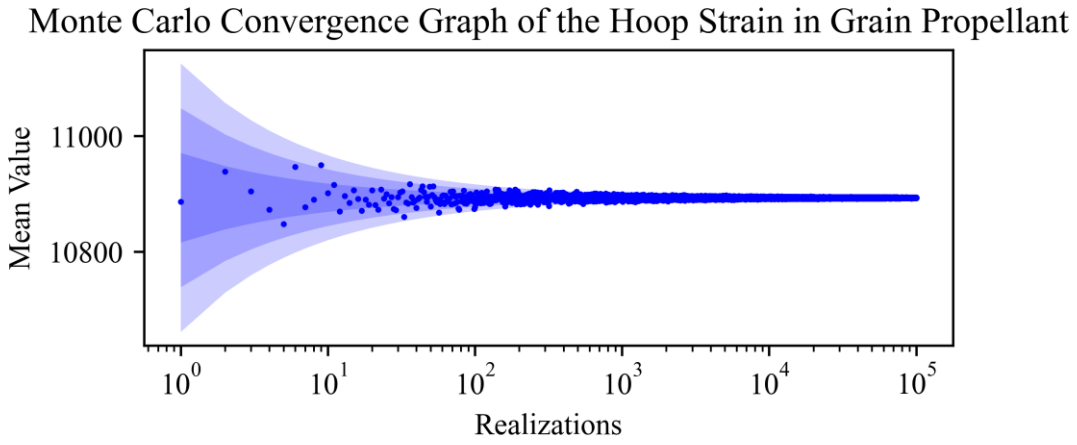

Figure 39: Convergence graph of Predicted Hoop Strains in Grain propellant.

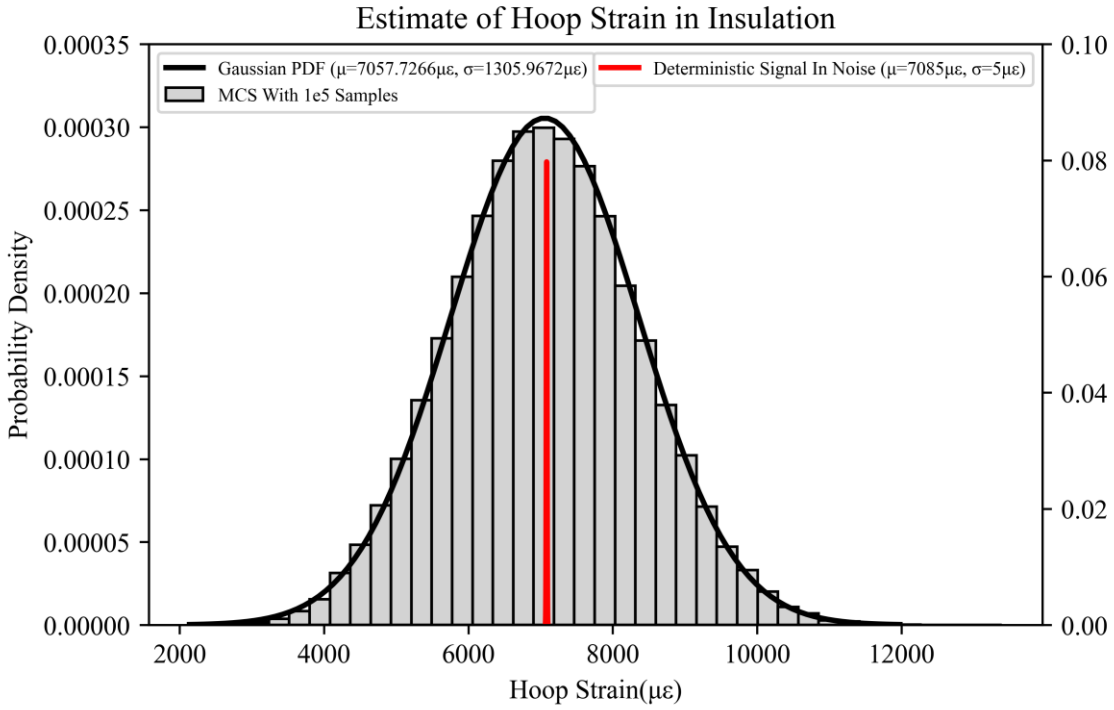

Figure 40: Predicted Hoop Strains distribution versus Deterministic Signal in Noise in Insulation.

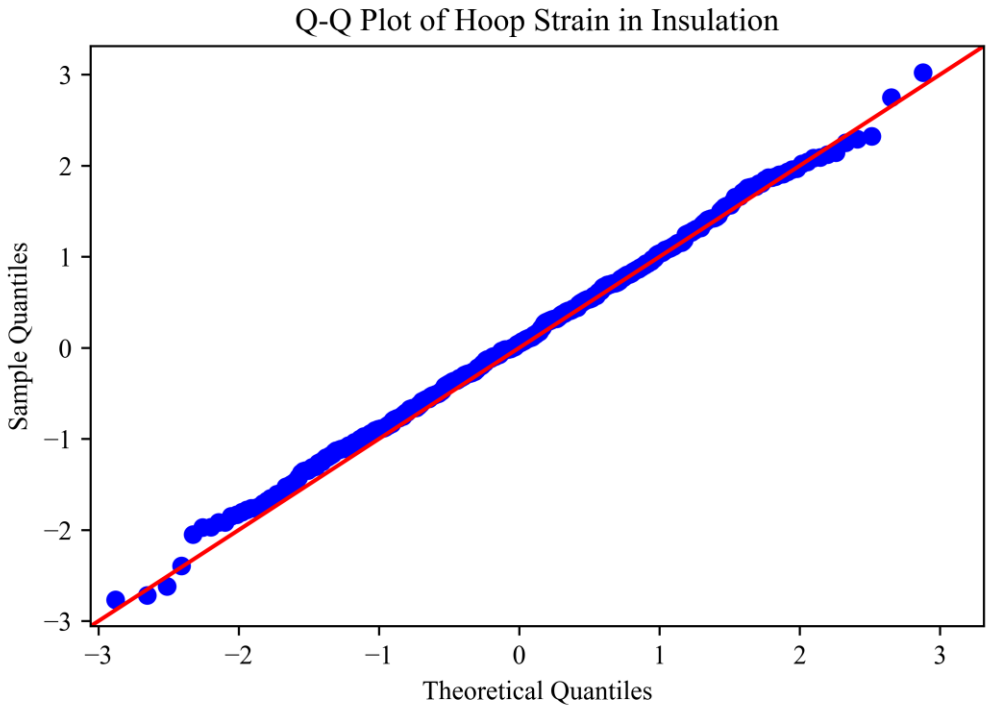

Figure 41: Q-Q plot of Predicted Hoop Strains in Insulation.

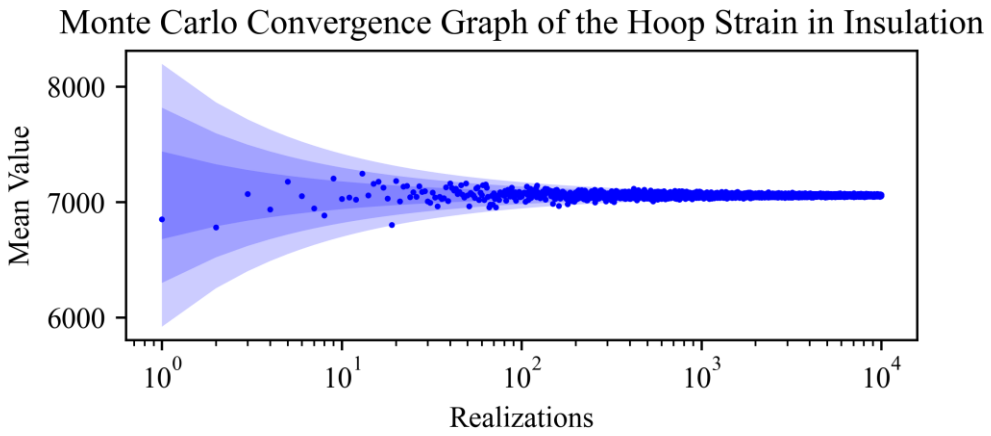

Figure 42: Convergence graph of Predicted Hoop Strains in Insulation.

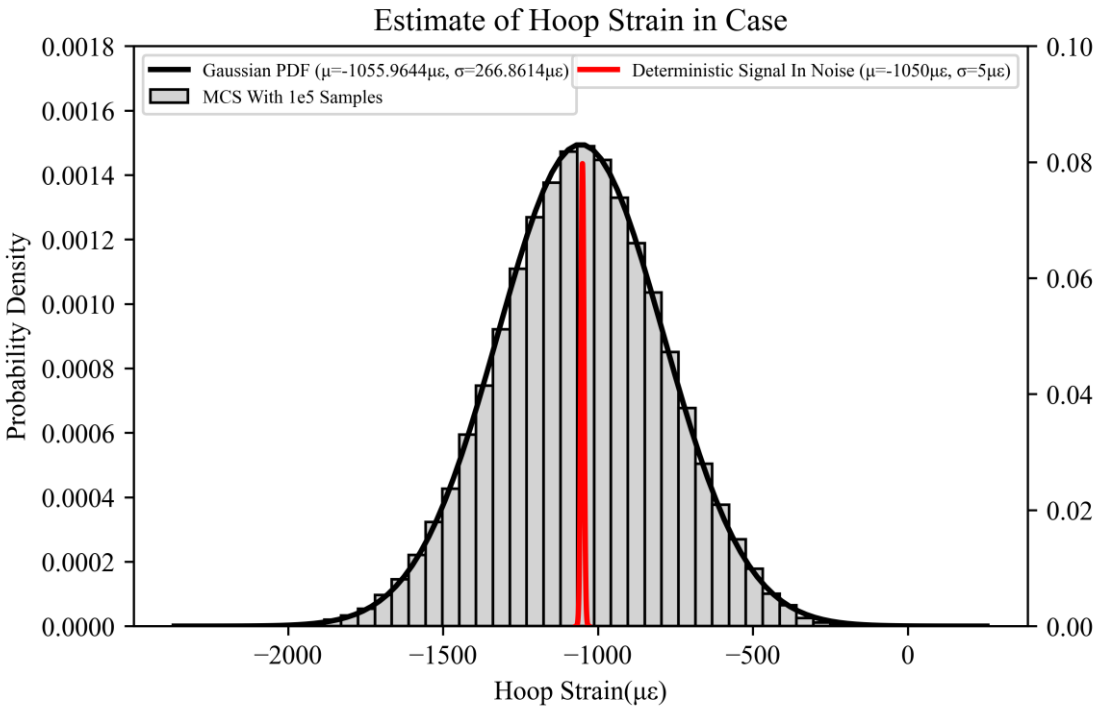

Figure 43: Predicted Hoop Strains distribution versus Deterministic Signal in Noise in Case.

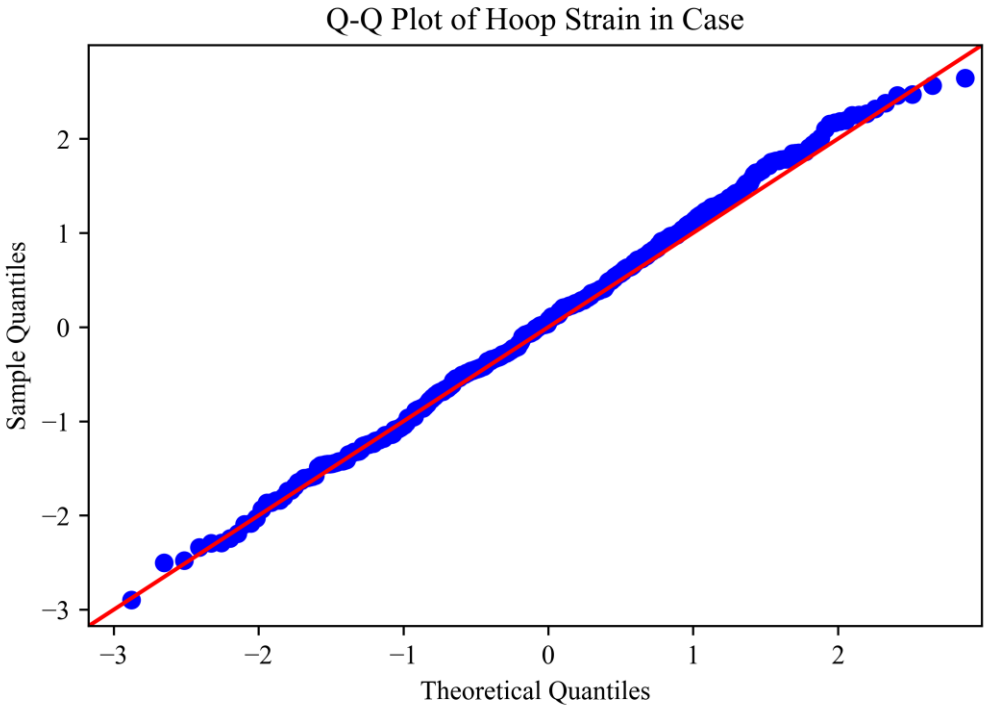

Figure 44: Q-Q plot of Predicted Hoop Strains in Case.

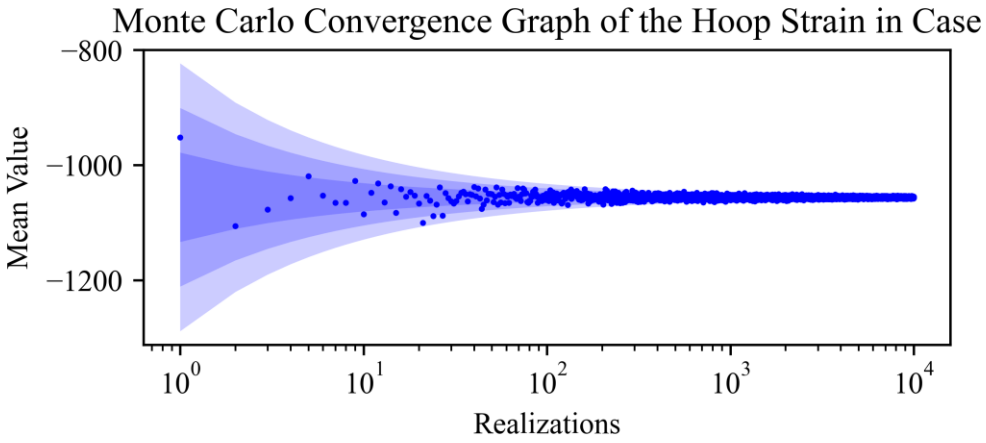

Figure 45: Convergence graph of Predicted Hoop Strains in Case.

Following the same process for the hoop strains of the damaged model, the respectively neural network is:

First layer and first hidden layer: Dense=512, activator: relu

Second hidden layer: Dense=256, activator: relu

Third hidden layer: Dense=128, activator: relu

Fourth hidden layer: Dense=64, activator: relu

Fifth hidden layer: Dense=32, activator: relu

Test size= 5%

Validation size= 10%

Batch size=32

Epochs=320

The performance of this neural network is shown in the 3 following graphs where it is clear that the loss of it is very low and the accuracy is close to 0.82.

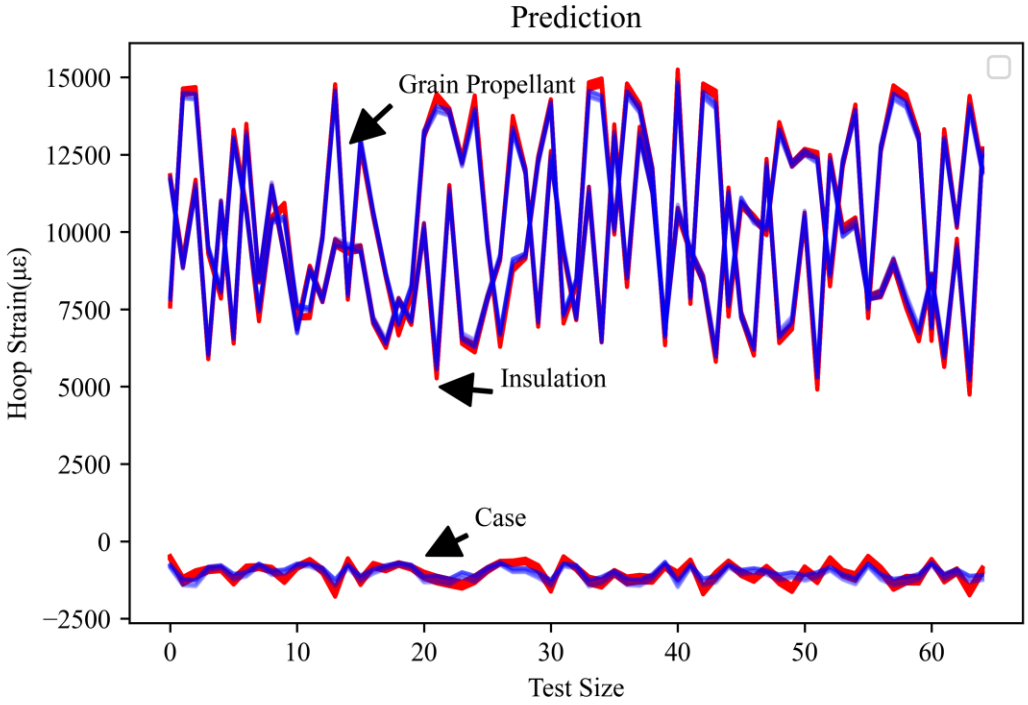

Figure 46: Prediction values versus actual values of the damaged model.

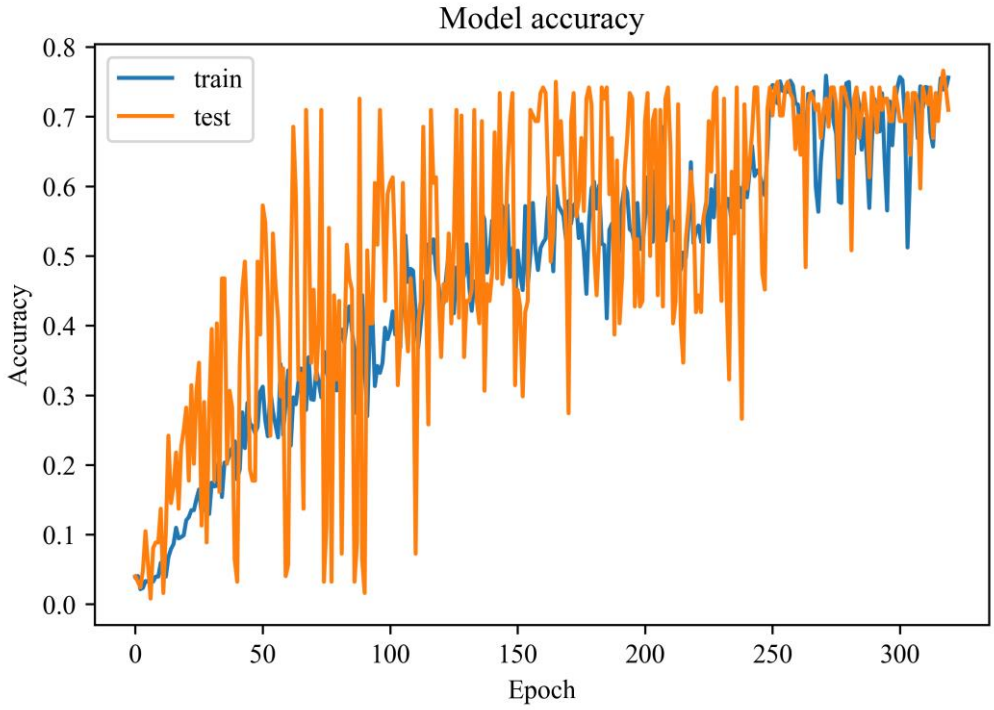

Figure 47: Accuracy of ANN for regression of the damaged model hoop strains.

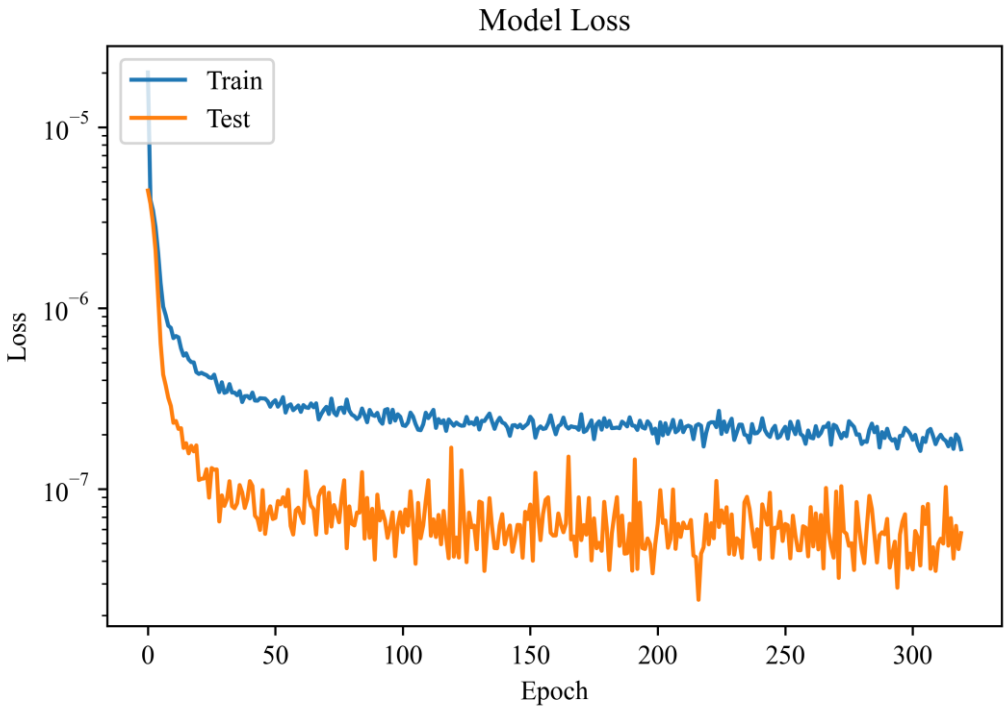

Figure 48: Loss of ANN for regression of the damaged model hoop strains.

Furthermore, the residual hoop strains for all the areas for 3 different angles are calculated and the respectively difference in standard deviation. The results are shown in figures 48 and 49 where the big difference between the healthy and the damaged model is located in the middle of the insulation. This data will be used on the same way as the data from the deterministic model to calculate the probability of detection.

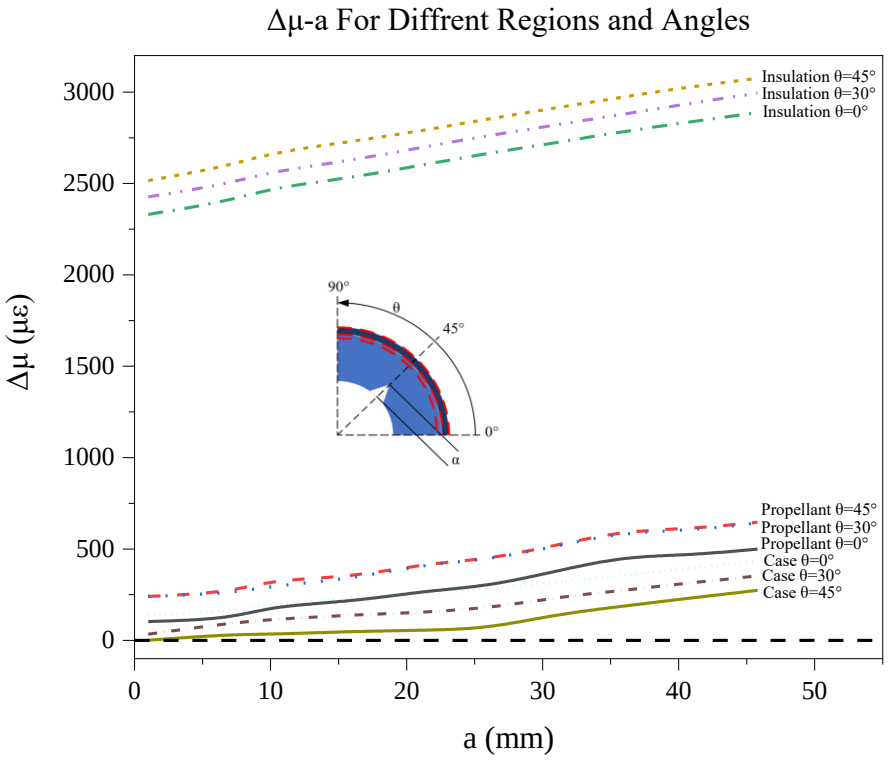

Figure 49: Residual Hoop Strain for different areas and angles.

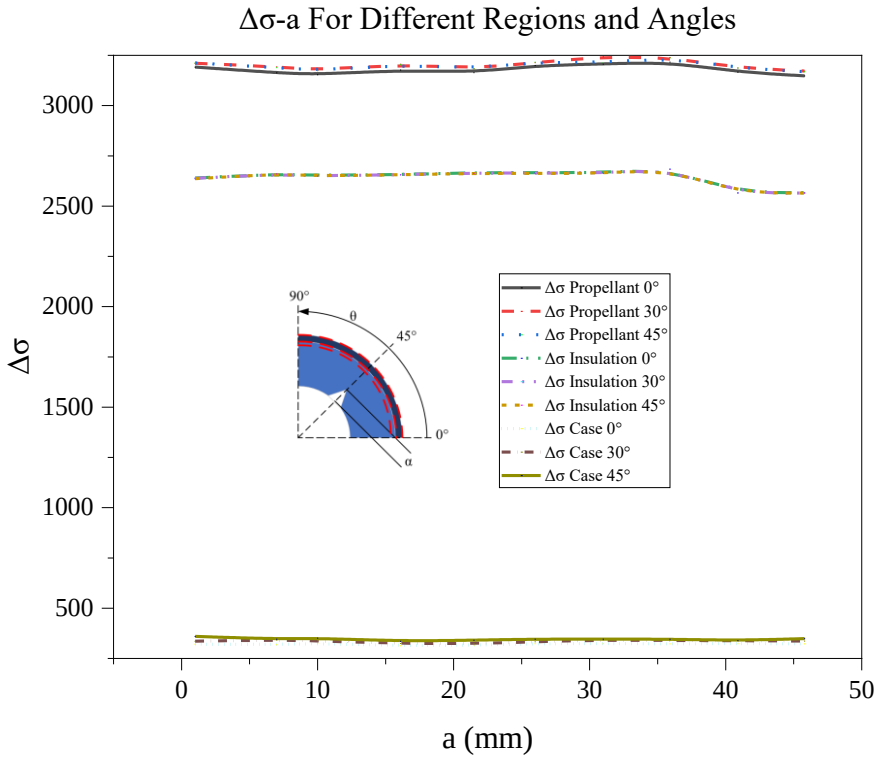

Figure 50: Difference in standard deviation for different areas and angles.

Because the results now have different mean values but also different standard deviations a new way to calculate probability of detection and probability of false alarm which is presented in the section II.c.

Using the equation (29) the P_D and P_{FA} are calculated for the three different areas and the ROC graphs also. From these figures, it is shown that the best results are located on the outer of the case and on the middle of the insulation but the performance of the detector was not high enough, so the placement of more sensors in each arc was considered crucial.

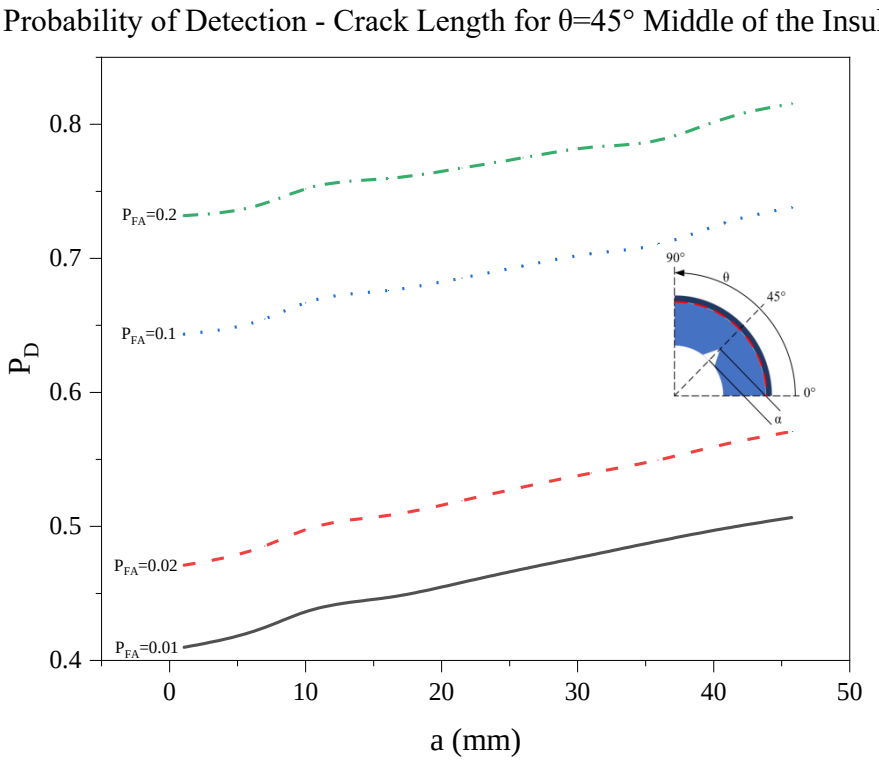

Figure 51: Probability of detection-Crack Length-Probability of false alarm Middle of the Insulation θ=45°.

In figure 51, it is shown that a single sensor that is placed on 45° on the middle of the insulation doesn't give good performance even for high probability of false alarm equal to 20%, where the best prediction is close to 80% of probability of detection for a crack of 45.8mm. This is shown also in figure 52, where for a specific probability of false alarm 0.01 the obtained probability of detection is lower than 50%, results that can't been taken into consideration due to the very low performance. Also, in figure 53, where the roc for one sensor on 45° on the middle of the insulation is plotted, it is evident that the performance has dropped dramatically in contrast to the rocs for the deterministic model.

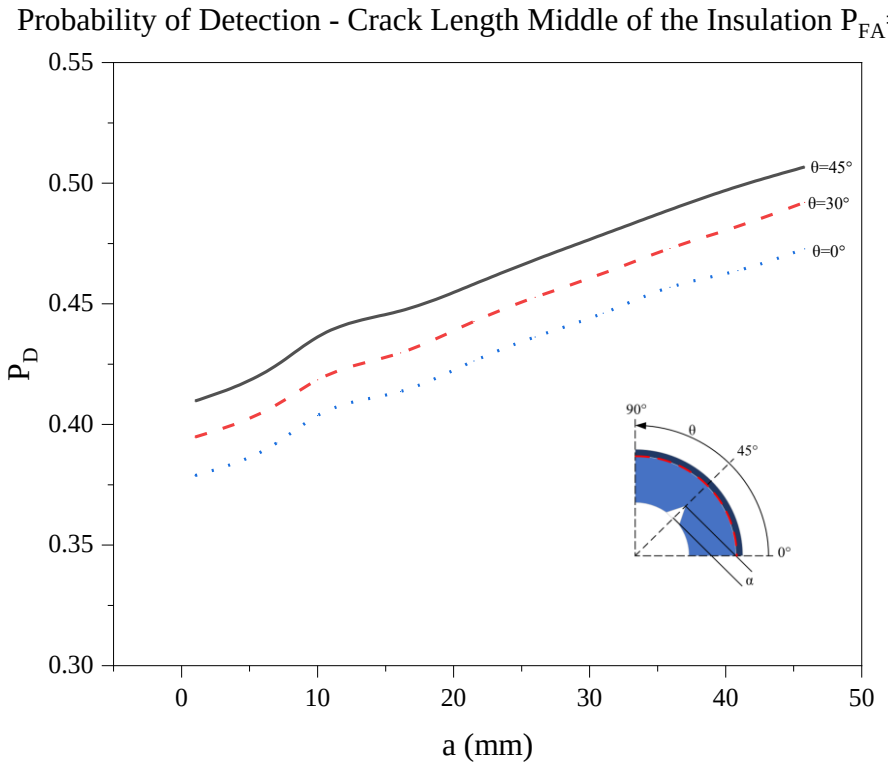

Figure 52: Probability of detection-Crack Length-Probability of false alarm-Degrees Middle of The Insulation.

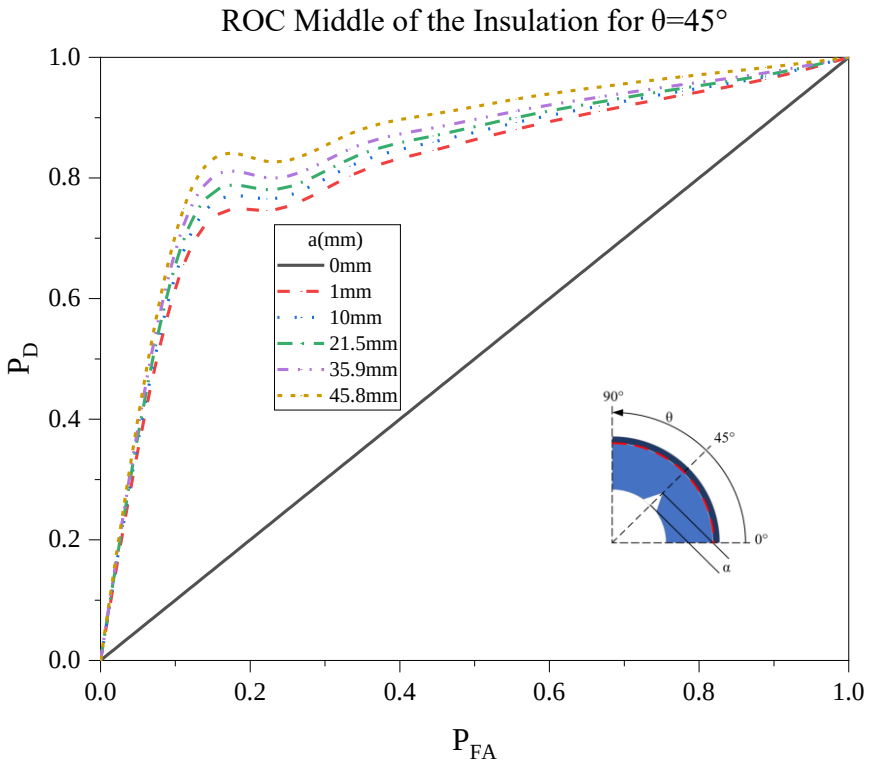

Figure 53: ROC Middle of the Insulation for θ=45°.

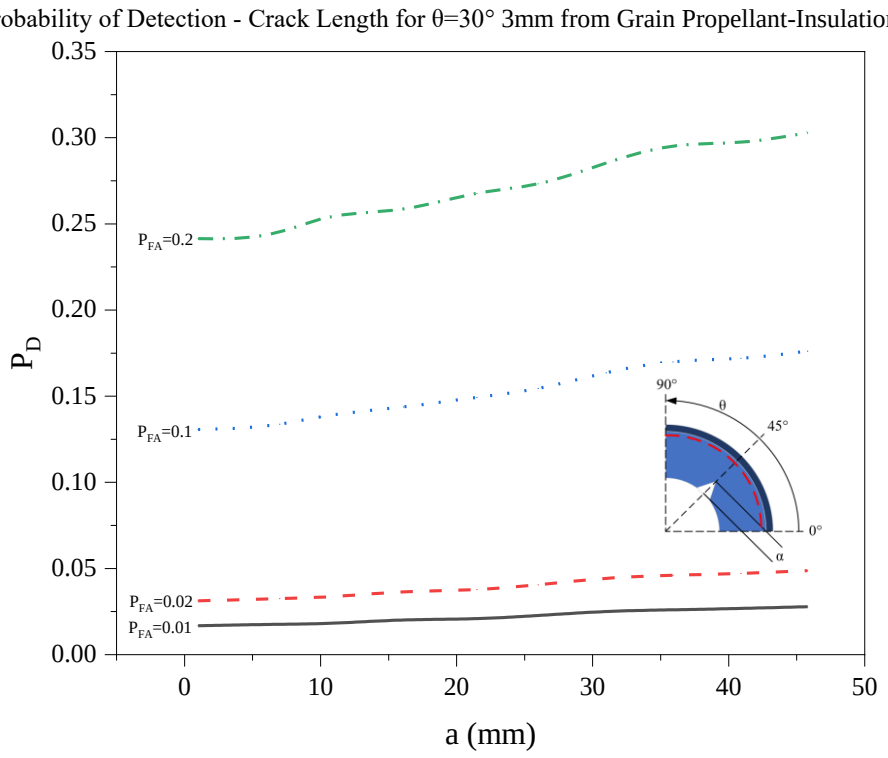

Figure 54: Probability of detection-Crack Length-Probability of false alarm of Grain propellant θ=30°.

Moving forward on the plotted results on 3mm from grain propellant and insulation interface it is clearly that placing a single sensor on this specific area doesn't seem to lead to sufficient information gain even for high probabilities of false alarm. This fact is confirmed also on the roc graph where it is shown the very low performance of the detector.

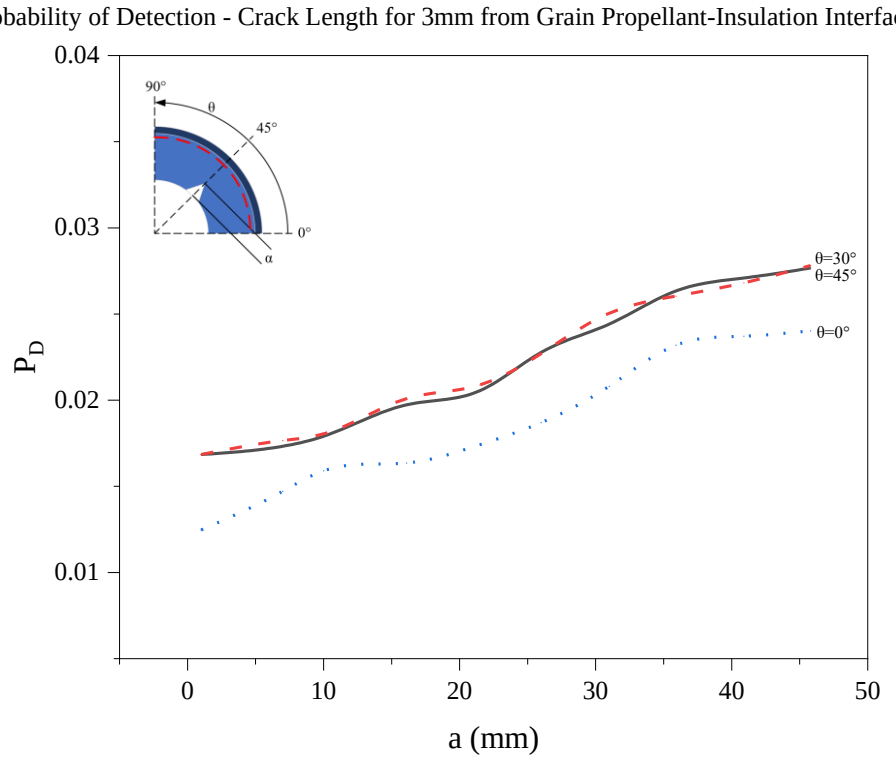

Figure 55: Probability of detection-Crack Length-Probability of false alarm-Degrees Grain propellant.

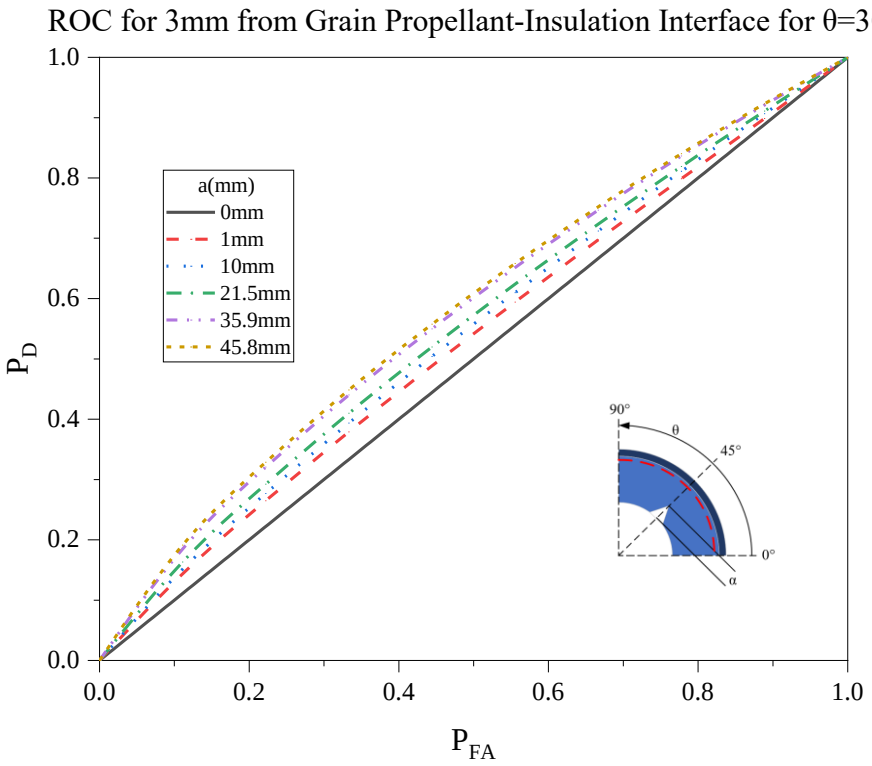

Figure 56: ROC Grain propellant for θ=30°.

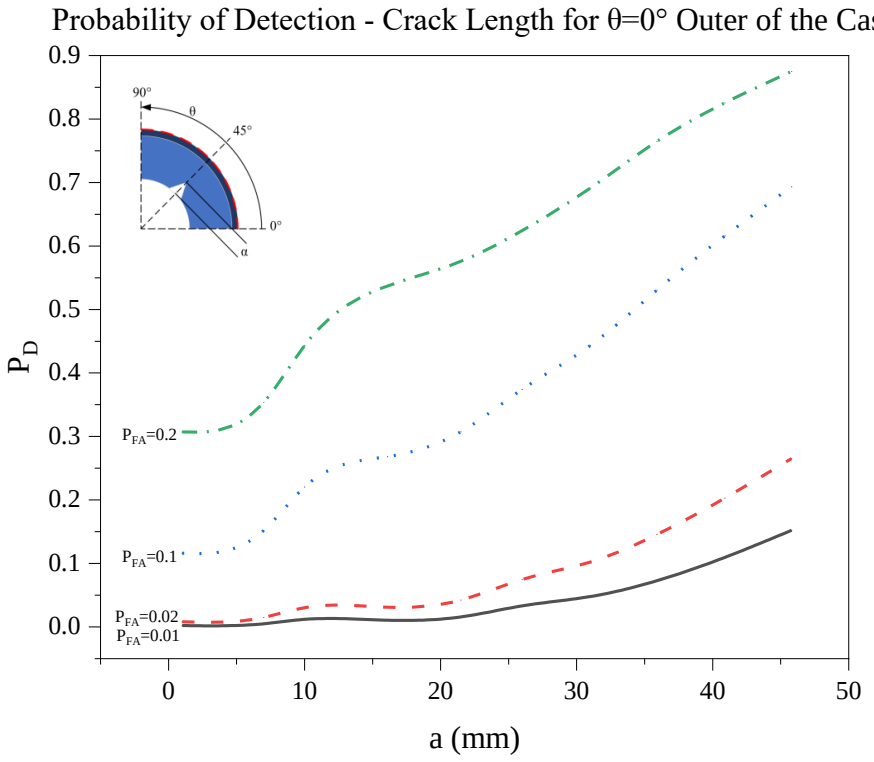

Figure 57: Probability of detection-Crack Length-Probability of false alarm of Outer of the Case θ=0°.

For the case of placing a sensor on 0° on the outer of the cylinder the detector give a 90% probability of detection for 20% probability of false alarm for a crack of 45.8mm but for a low P_{FA} , as it is shown in figure 58, the probability of detection is again very low. The roc graph on this case gives better results than the cases of grain propellant and insulation.

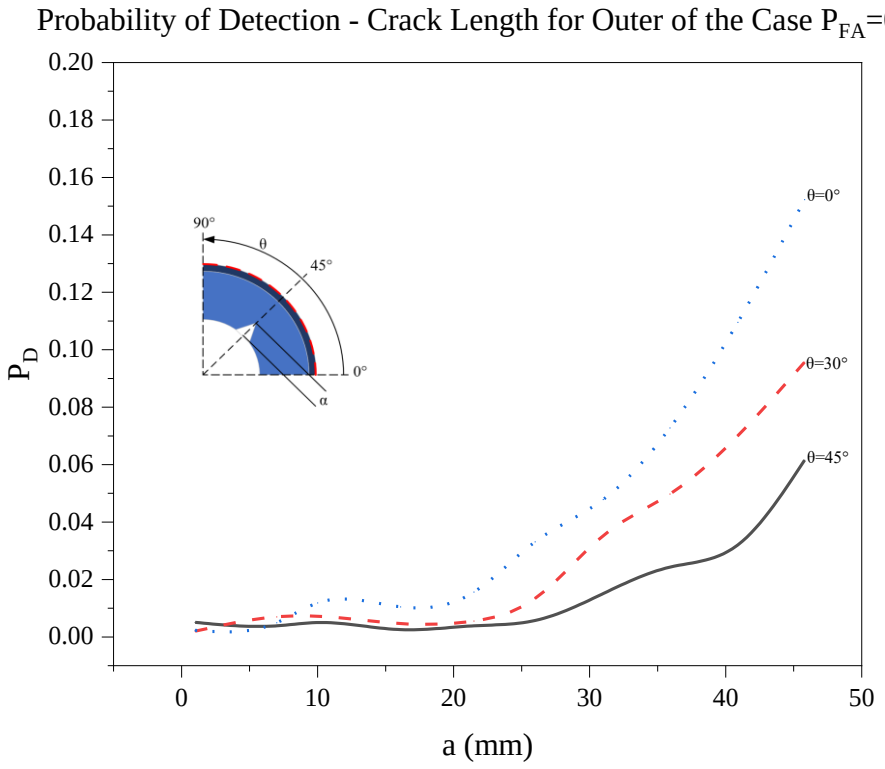

Figure 58: Probability of detection-Crack Length-Probability of false alarm-Degrees Outer of the Cylinder.

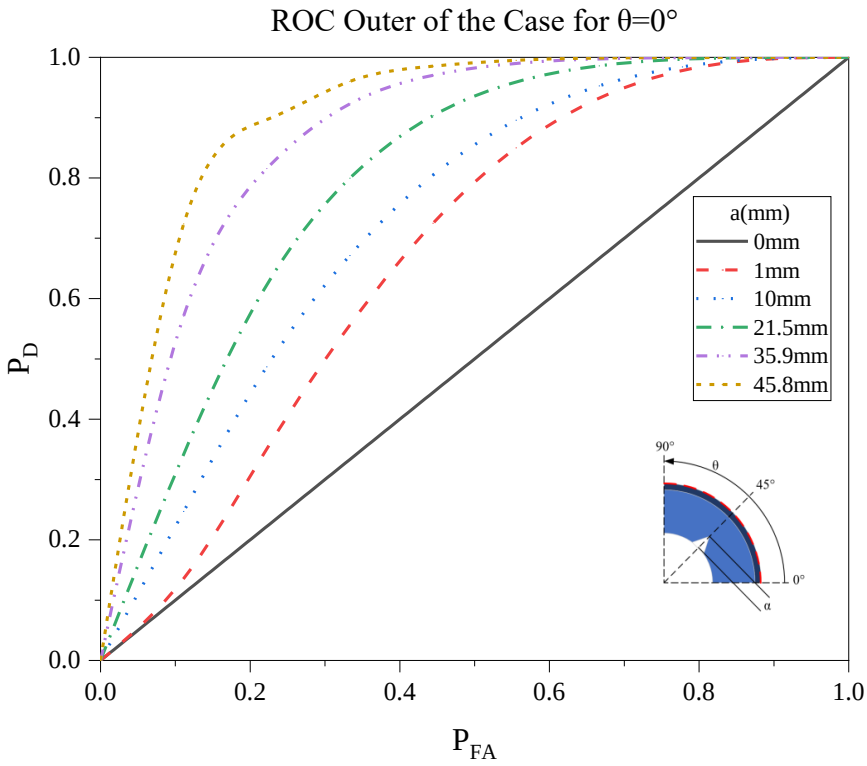

Figure 59: ROC Outer of the Cylinder for θ=0°.

For the case of the uncertainty propagation, one sensor through an arc was not enough to obtain a good probability of detection for a small probability of false alarm, so it was important to place more sensors. The addition of multiple sensors provides (hopefully) additional informative features that, when combined, increase knowledge of the system's state of nature. This information gain is expected to increase the discriminant power of the hypothesis test, which is then quantified by an increase in accuracy. The ROC curves for this case were derived using Equations (30) and (31). In the following figures, there are presented the ROC graphs for 1,3,6 and 9 sensors for hoop strains on the outer of the cylinder and middle of the insulation and 3mm from grain propellant insulation interface.

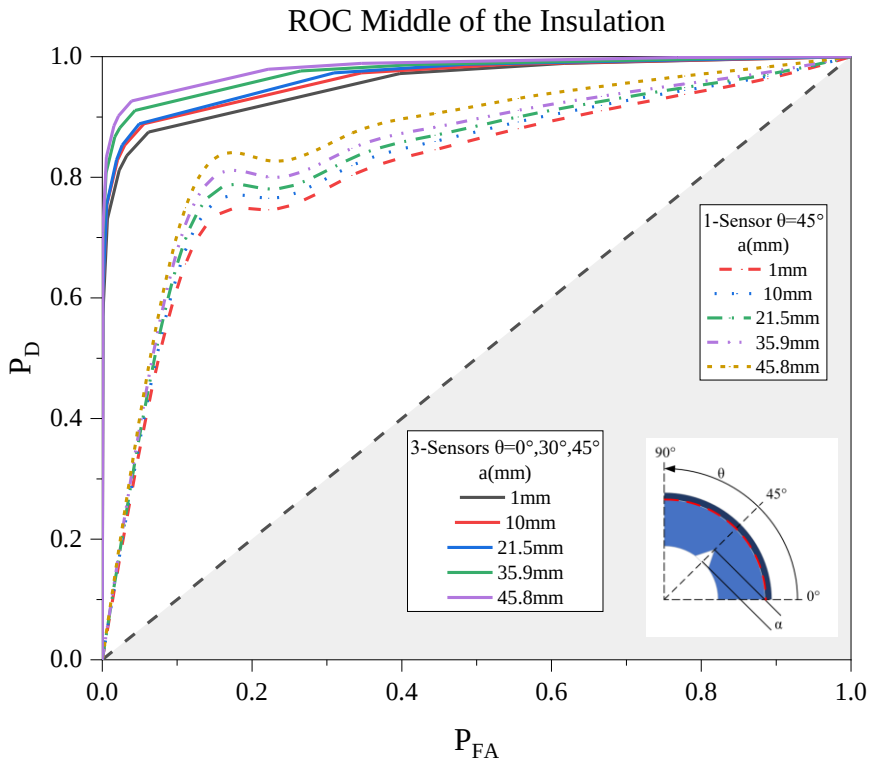

Figure 60: ROC Middle of the Insulation for 1 and 3 Sensors.

In figure 60, it is evident that placement of 3 sensors on 0°,30°,45° on the middle of the insulation increases dramatically the performance of the detector and so it is possible to detect smaller cracks. On the other hand, placing 3 sensors on 3mm from grain propellant insulation interface doesn't increase enough the performance of the detector. Last, placing 3 sensors on the grain propellant, also, increases the performance in contrast to figure's 59 results.

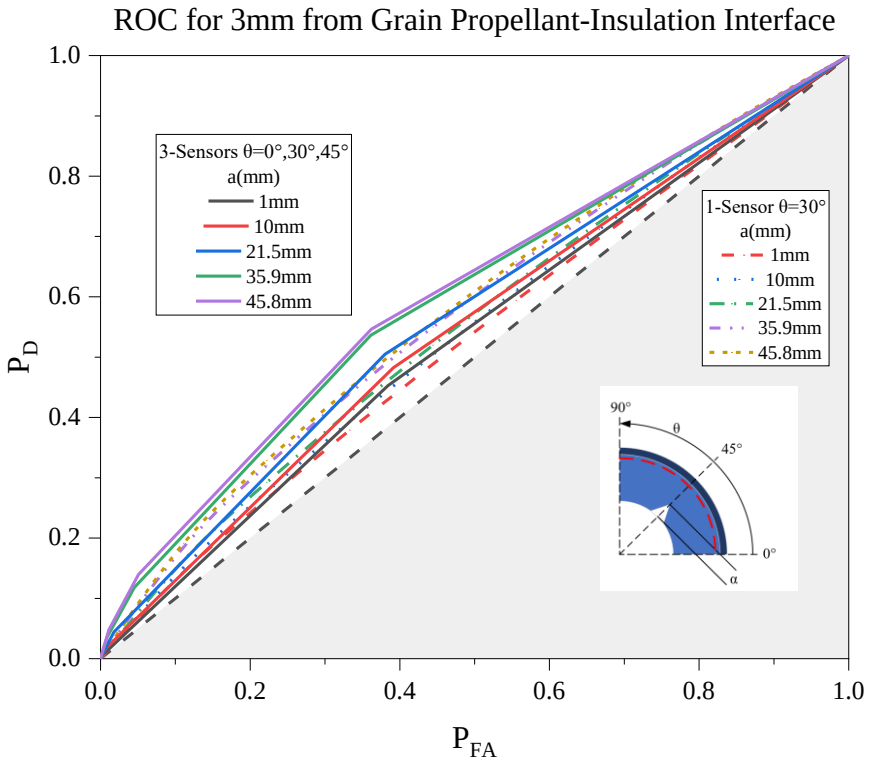

Figure 61: ROC Grain propellant for 1 and 3 Sensors.

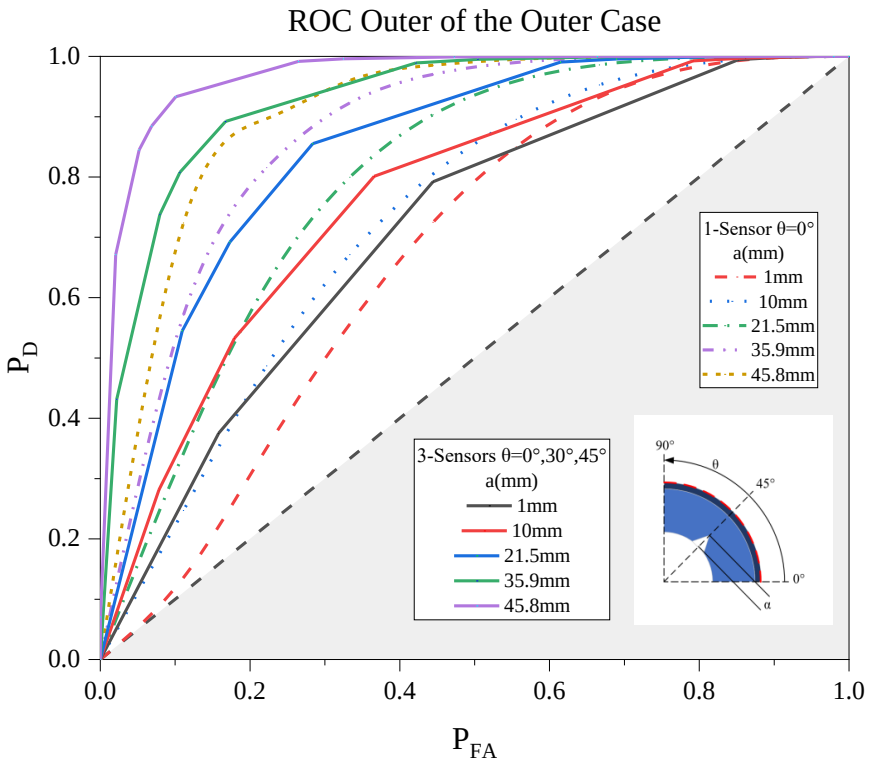

Figure 62: ROC Outer of the Cylinder for 1 and 3 sensors.

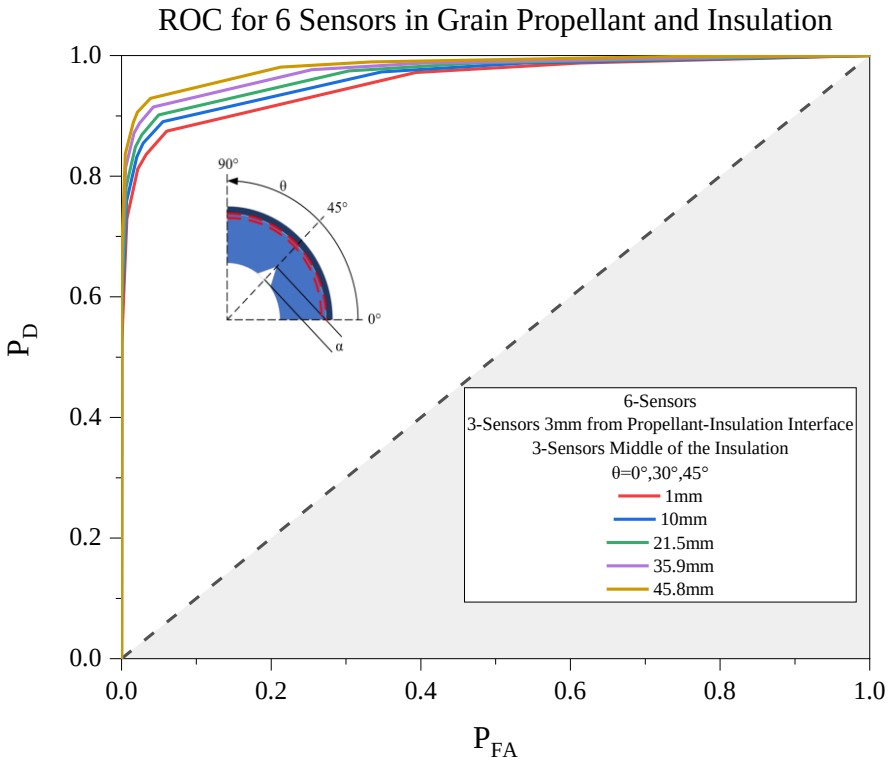

Figure 63: ROC Grain propellant and Middle of the Insulation for 6 sensors.

Furthermore, the placement of 6 sensor system with 3 sensors on grain propellant and another 3 on the insulation and a system with 3 sensors on insulation and another 3 on case is analyzed, and the better performance it is gained from the system on case and insulation and the detection capability is increased in contrast to 3 sensor systems. Adding now additional 3 sensors on the grain propellant to the previous optimal system the detector's performance doesn't add some extra value to the detector's performance. So the best solution is the placement of 3 sensors on case and another 3 on the insulation.

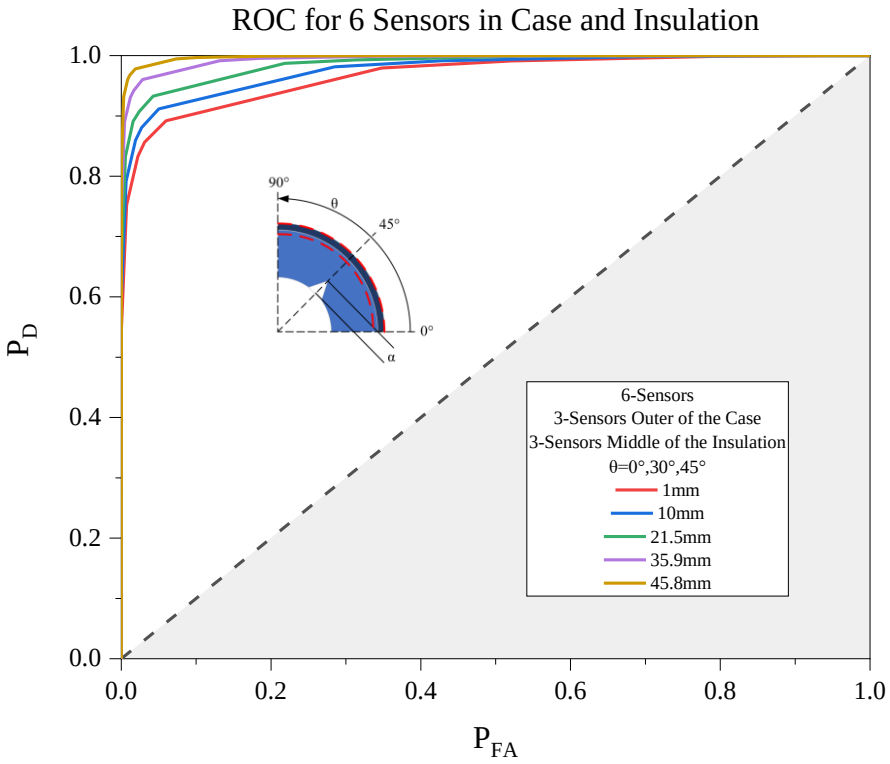

Figure 64: ROC Outer of the Cylinder and Middle of the Insulation for 6 sensors.

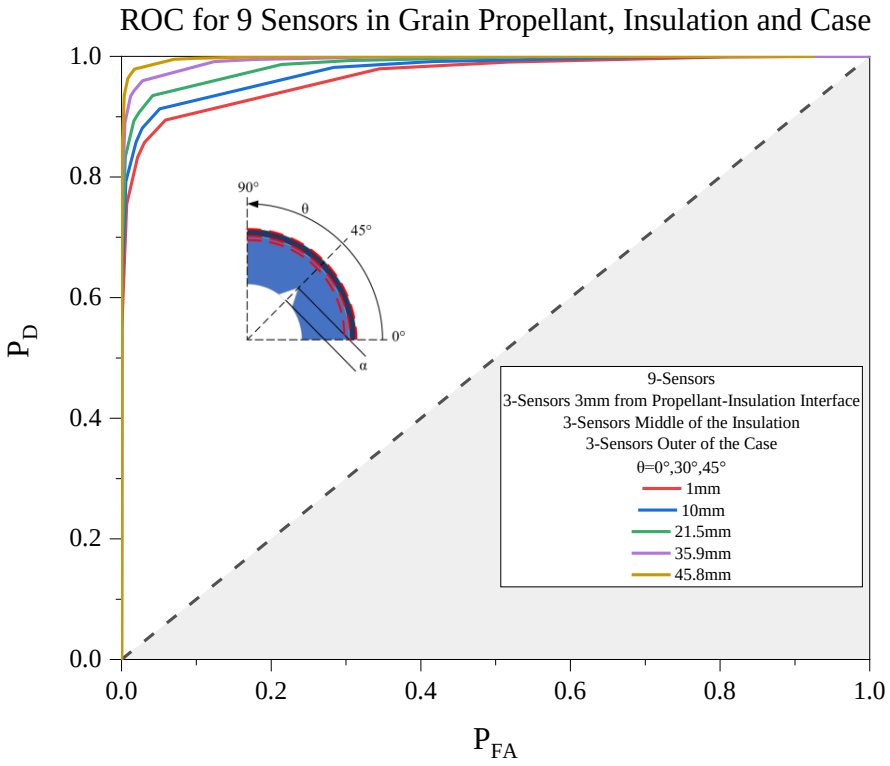

Figure 65: ROC Outer of the Cylinder, Middle of the Insulation and Grain propellant for 9 sensors.

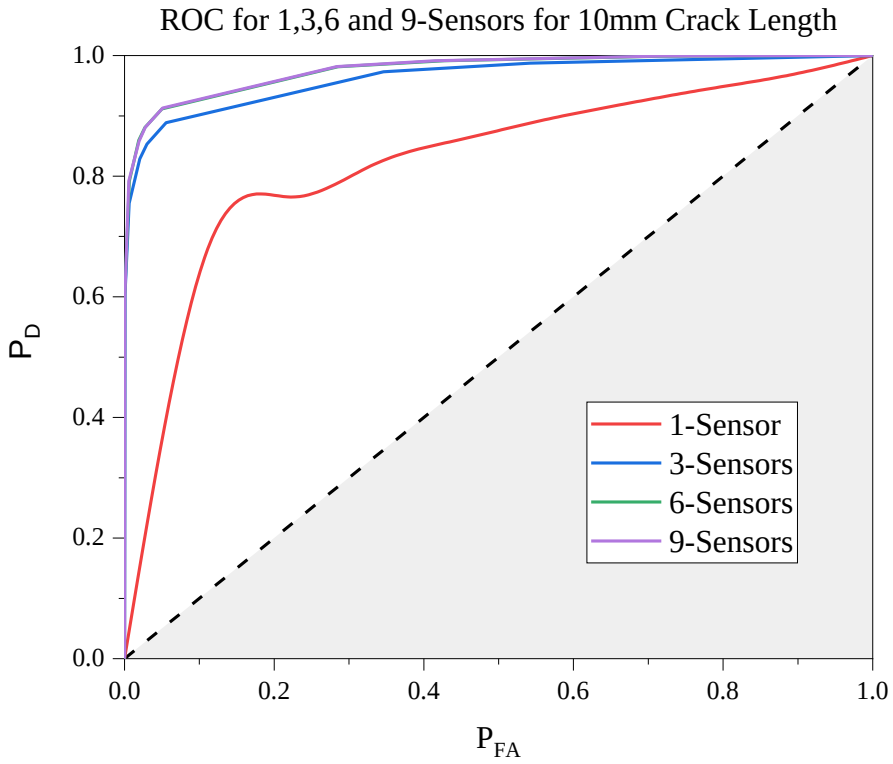

Figure 66: ROC for 1,3,6 and 9 sensors for 10mm crack length.

Also, in figure 67, it can be seen the various probabilities of detection for different crack lengths for probability of false alarm 0.01 and 3,6 and 9 sensors. The fact that the additional 3 sensors on the 6 sensor system doesn't add any useful information it is clear in this graph where the curve of 6 and 9 sensors if exactly the same.

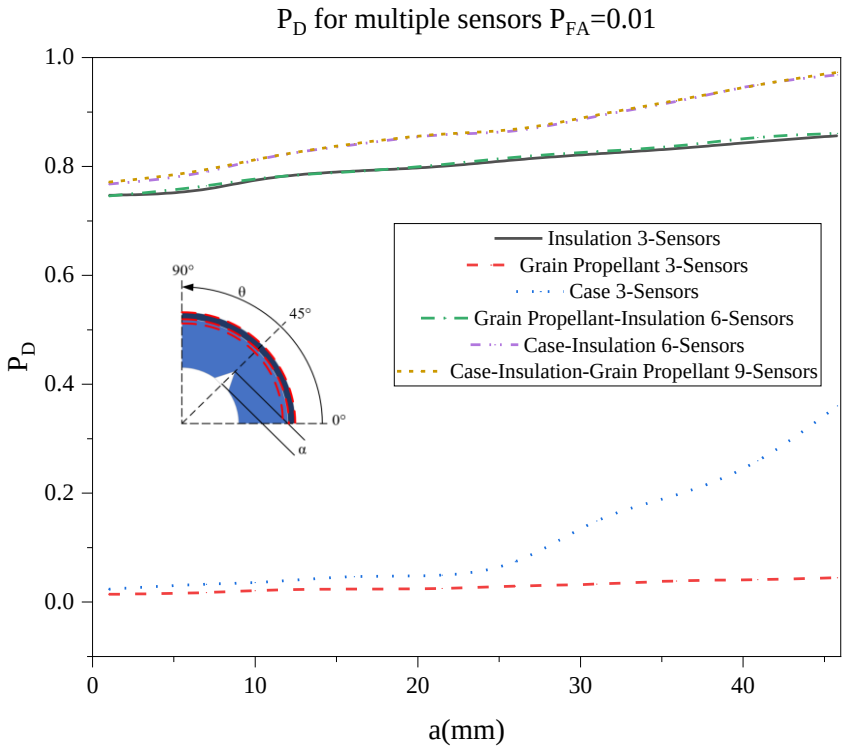

Figure 67: Probability of detection-Crack Length-Probability of false alarm-Sensors.

As a conclusion of all the above graphs, the placement of 3 sensors in middle of insulation and another 3 on the outer of the cylinder is the optimal to detect smaller crack lengths with higher probability of detection.

VII. Concluding Remarks

Structural health monitoring is crucial to detect cracks in solid rocket motors. The method that is analyzed in this thesis compares the data of the damaged model with the healthy one, using finite element analysis with the ANSYS APDL software package. One sensor is considered enough for the deterministic case to detect small crack lengths with high probability of detection in case where the material properties are treated as uncertainties, occasion which is closer to the real world. However, it is shown that a system of 6 sensors, located in the middle of the insulation and outer of the cylinder, optimizes the detection performance of the system.

VIII. Connection points of thesis subject with Marine sector

In this thesis we deal with the study of cracks in SRMs, that are usually made of composite materials and for all of them a Structural Health Monitoring system has been established to monitor their health and evaluate it. But these methods can easily be transferred to the shipbuilding sector where cracks can appear in the construction of a ship, lot of ships are constructed from composite materials, and the SHM method is critical to them to evaluate and monitor their health in order to avoid different failures in their construction and to avoid accidents which will have economical losses and possibly human life losses.

IX. References

1. M. Gruntman: Chapters 1-2, Blazing the trail: the early history of spacecraft and rocketry.

2. C. Riziotis, L. Eineder, L. Bancallari, G. Tussiwand, "Structural health monitoring of solid rocket motors' propellant using polymer optical fibers", Key Engineering Materials, 543, 360-363, (2013).

3. C. Riziotis, L. Eineder, L. Bancallari, G. Tussiwand, "Fiber optic architectures for strain monitoring of solid rocket motors' propellant", Sensor Letters, 11(8), 1403-1407 (2013).

4. https://en.wikipedia.org/wiki/Space_Shuttle_Solid_Rocket_Booster

5. M. Marquis: Stress Analysis and Structural Diagnosis of Solid Rocket Motors Using Finite the Element Method (2021) Link: https://escholarship.org/uc/item/2cf5h8gd

6. S. Rajesh, G. Suresh and R. Chandra Mohan: A Review on Material Selection and Fabrication of Composite Solid Rocket Motor (SRM) Casing (2017)

7. Anhduong Q. Le, A.M. ASCE; L. Z. Sun, Ph.D., M. ASCE; and Timothy C. Miller, Ph.D. (2015): Health Monitoring and Diagnosis of Solid Rocket Motors with Grain propellant Cracks DOI: 10.1061/(ASCE)AS.1943-5525.0000556.

8. Anhduong Q. Le and L. Z., Irvine and Timothy C. Miller (2013): Detectability of Delaminations in Solid Rocket Motors with Embedded Stress Sensors DOI: 10.2514/1.B34523.

9. D. Liu and L. Sun and Timothy C. Miller (2020): Defect Diagnosis in Solid Rocket Motors Using Sensors and Deep Learning Networks Link: https://doi.org/10.2514/1.J059600.

10. R. Ranganathan (1999): Structural Reliability Analysis and Design.

11. J. Zhang (2020): Modern Monte Carlo Methods for Efficient Uncertainty Quantification and Propagation: A Survey.

12. P. H. Chou, K. N. Chiang and Steven Y. Liang (2022): RELIABILITY ASSESSMENT OF WAFER LEVEL PACKAGE USING ARTIFICIAL NEURAL NETWORK REGRESSION MODEL

13. C. Riziotis and A. Vasilakos, "Computational intelligence in photonics technology and optical networks: A survey and future perspectives", Information Sciences 177, 5292 (2007).

14. Ronald E. Walpole, Raymond H. Myers, Sharon L. Myers, K. Ye: Probability & Statistics for Engineers & Scientists NINTH EDITION.

15. Kay S. M. Fundamentals of Statistical Signal Processing Volume II: Detection Theory, Prentice Hall (1998).

16. D. Liu, L. Sun and Timothy C: Defect Diagnosis in Solid Rocket Motors Using Sensors and Deep Learning Networks. Link: https://arc.aiaa.org/doi/10.2514/1.J059600.

17. Dr. A.-V. Phan: ANSYS TUTORIAL – 2-D Fracture Analysis.

18. Least Square Fitting Wolfram MathWorld.Link:**https://mathworld.wolfram.com/LeastSquaresFitting.html**

19. R-Squared vs. Adjusted R-Squared: What's the Difference? Investopedia. Link: https://www.investopedia.com/ask/answers/012615/whats-difference-between-rsquared-and-adjusted-rsquared.asp